

# Measurements of the Quasi-Elastic and Elastic Deuteron Tensor Asymmetries v. 0.907

---

A Proposal to Jefferson Lab PAC 43  
(Update to LOI12-14-002)

E. Long,<sup>†‡</sup> K. Slifer,<sup>†</sup> P. Solvignon,<sup>†</sup> T. Badman, S. Li, K. McCarty, C. Meditz, M.  
O'Meara, R. Paremuzyan, S. Santiesteban, B. Yale, R. Zielinski  
*University of New Hampshire, Durham, NH 03861*

D. Day,<sup>†</sup> D. Keller,<sup>†</sup> D. Crabb, S. Liuti, O. A. Rondon, V. Sulkosky  
*University of Virginia, Charlottesville, VA 22903*

D. Higinbotham<sup>†</sup>, A. Camsonne, D. Gaskell  
*Thomas Jefferson National Accelerator Facility, Newport News, VA 23606*

Z. Ye  
*Duke University, Durham, NC 27708*

N. Kalantarians  
*Hampton University, Hampton, VA 23668*

A. Ahmidouch, S. Danagoulian  
*North Carolina A&T State University, Greensboro, NC 27411*

M. Sargsian  
*Florida International University, Miami, FL 33199*

M. Strikman  
*Pennsylvania State University, University Park, PA 16802*

G. A. Miller  
*University of Washington, Seattle, WA 98195*

---

<sup>†</sup>Spokesperson

<sup>‡</sup>Contact: ellie@jlab.org

## Abstract

In this update to LOI12-14-002, we propose the first measurement of the tensor asymmetry  $A_{zz}$  in the quasi-elastic region through the tensor polarized  $D(e, e')X$  channel; an asymmetry that is sensitive to the nucleon-nucleon potential. Previous measurements of  $A_{zz}$  have been used to extract  $b_1$  in the DIS region and  $T_{20}$  in the elastic region. In the quasi-elastic region,  $A_{zz}$  has not previously been measured. The measurements described in this proposal push the limits of understanding the deuteron by entering kinematics that haven't been measured and where current theoretical understanding is weak.

$A_{zz}$  was first calculated in 1988 by Frankfurt and Strikman, using the Hamada-Johnstone and Reid soft-core wave functions [1]. Recent calculations by M. Sargsian and M. Strikman revisit  $A_{zz}$  in the  $x > 1$  range using virtual-nucleon and light-cone methods, which differ by up to a factor of two [2] and can be discriminated experimentally at the  $3 - 6\sigma$  level. Additionally, the calculations were done using multiple deuteron wavefunctions which show a large discrepancy at high  $x$ . Effects from final state interactions have also been calculated using a virtual nucleon model with various NN potentials by W. Cosyn, which have a are expected to have significant effect on  $A_{zz}$  at large  $x$ .

One of the leading uncertainties that will effect all tensor polarized deuterium experiments is the absolute knowledge of the tensor polarization. We have found that by using the elastic reaction at low  $Q^2$ , we can normalize our target's degree of polarization to the high precision and low  $Q^2$  NIKHEF measurement. The NIKHEF tensor polarization was created with an atomic beam source and they were able to measure the polarization of the gas with both a Briet-Rabi polarimeter as well as an ion-extraction polarimeter.

The kinematic requirements of  $A_{zz}$  allow for the simultaneous measurement of elastic  $T_{20}$  at multiple  $Q^2$  points ranging from  $0.2 < Q^2 < 1.8 \text{ GeV}^2$ , the largest range ever for a single  $T_{20}$  experiment. At low  $Q^2 \sim 0.2 \text{ GeV}^2$ ,  $T_{20}$  is well known experimentally and theoretically making it an ideal calibration point to reduce uncertainty from target polarization, as mentioned above. At mid  $Q^2 \sim 0.7 \text{ GeV}^2$ , we will take a high-precision measurement in the region where previous JLab Hall C results systematically disagree with results from MIT-Bates. Finally, at high  $Q^2 \sim 1.5$  and  $1.8 \text{ GeV}^2$  we will measure  $T_{20}$  up to the largest momentum transfer yet while providing a crucial check of the only existing data at large  $Q^2 > 1$ , which systematically differs from other results at lower  $Q^2$ .

We propose an experimental determination of  $A_{zz}$  and  $T_{20}$  utilizing the same equipment as the E13-12-011  $b_1$  experiment. Six different  $Q^2$  values of  $A_{zz}$  and four of  $T_{20}$  will be measured over the course of 34 days, with 10.3 additional days of overhead. The proposed  $A_{zz}$  measurements are more than an order of magnitude less sensitive to systematic uncertainties than E13-12-011, so this experiment could also be utilized to better understand the in-beam conditions and time-dependent systematic effects of a tensor polarized target for the  $b_1$  experiment.

# Contents

|    |          |   |           |
|----|----------|---|-----------|
| 63 |          |   |           |
| 64 | <b>1</b> | <b><math>A_{zz}</math> Motivation</b>               | <b>4</b>  |
| 65 | 1.1      | Probing the Deuteron Wavefunction . . . . .         | 5         |
| 66 | 1.2      | Study of the Relativistic NN Bound System . . . . . | 6         |
| 67 | 1.3      | Interest from Theorists . . . . .                   | 7         |
| 68 | <b>2</b> | <b><math>T_{20}</math> Motivation</b>               | <b>8</b>  |
| 69 | <b>3</b> | <b>The Proposed Experiment</b>                      | <b>9</b>  |
| 70 | 3.1      | $A_{zz}$ Experimental Method . . . . .              | 10        |
| 71 | 3.2      | $T_{20}$ Experimental Method . . . . .              | 12        |
| 72 | 3.3      | Kinematics . . . . .                                | 13        |
| 73 | 3.4      | Uncertainty Estimates . . . . .                     | 20        |
| 74 | 3.4.1    | Statistical Uncertainty . . . . .                   | 20        |
| 75 | 3.4.2    | Systematic Uncertainty . . . . .                    | 21        |
| 76 | 3.4.2.1  | Time Dependent Factors . . . . .                    | 23        |
| 77 | 3.4.2.2  | Drift Mitigation . . . . .                          | 24        |
| 78 | 3.4.2.3  | Trigger-Tracking . . . . .                          | 25        |
| 79 | 3.4.2.4  | Target Dilution and Length . . . . .                | 26        |
| 80 | 3.4.2.5  | Solid Angle . . . . .                               | 27        |
| 81 | 3.4.2.6  | Beam Current Monitors . . . . .                     | 28        |
| 82 | 3.4.2.7  | Systematic Summary . . . . .                        | 28        |
| 83 | 3.5      | Polarized Target . . . . .                          | 28        |
| 84 | 3.5.1    | Polarization Analysis . . . . .                     | 30        |
| 85 | 3.5.2    | Tensor Polarization Enhancement . . . . .           | 31        |
| 86 | 3.5.3    | Depolarizing the Target . . . . .                   | 31        |
| 87 | 3.5.4    | Dilution Factor . . . . .                           | 31        |
| 88 | 3.6      | Overhead . . . . .                                  | 33        |
| 89 | <b>4</b> | <b>PAC42 Comments and Concerns</b>                  | <b>33</b> |
| 90 | 4.1      | Theory Advisory Committee . . . . .                 | 33        |
| 91 | 4.2      | Technical Advisory Committee . . . . .              | 34        |
| 92 | 4.3      | Program Advisory Committee . . . . .                | 35        |
| 93 | 4.4      | Response to PAC42 Concerns . . . . .                | 35        |
| 94 | <b>5</b> | <b>Summary</b>                                      | <b>36</b> |

# 1 $A_{zz}$ Motivation

The deuteron is the simplest composite nuclear system, and in many ways it is as important to understanding bound states in QCD as the hydrogen atom was to understanding bound systems in QED. Our experimental and theoretical understanding of the deuteron remains unsatisfying, which we will address by measuring the tensor asymmetry  $A_{zz}$  for the first time in a kinematic region where theoretical understanding of the deuteron is weak.

Due to their small size and simple structure, tensor polarized deuterons are ideal for studying nucleon-nucleon interactions. Tensor polarization enhances the D-state contribution, which compresses the deuteron [3], making the system more sensitive to short-range QCD effects. Understanding the nucleon-nucleon potential of the deuteron is essential for understanding short-range correlations as they are largely dependent on the tensor force [4]. We can resolve the short-range structure of nuclei on the level of nucleon and hadronic constituents by utilizing processes that transfer to the nucleon constituents both energy and momentum larger than the scale of the NN short-range correlations, particularly at  $Q^2 > 1 \text{ (GeV/c)}^2$ .

By taking a ratio of cross sections from electron scattering from tensor-polarized and unpolarized deuterons,

$$A_{zz} = \frac{2}{fP_{zz}} \left( \frac{\sigma_p}{\sigma_u} - 1 \right), \quad (1)$$

the S and D-wave states can be disentangled, leading to a fuller understanding of the repulsive nucleon core. A measurement of  $A_{zz}$  is sensitive to the ratio  $\frac{D^2 - SD}{S^2 + D^2}$  and its evolution with increasing minimal momentum of the struck nucleon. Originally calculated by L. Frankfurt and M. Strikman [1], this has recently been revisited by M. Sargsian and M. Strikman, who calculated  $A_{zz}$  in this region using light cone and virtual nucleon approaches with multiple NN potentials [5]. The calculations vary by up to a factor of 2, and can be experimentally determined at the  $3 - 6\sigma$  level as discussed in this proposal. In this same region, effects from final state interactions have been calculated and are expected to have a significant effect at large  $x$  [6].

For the lower  $Q^2$  region, W. Van Orden has calculations in progress using different nucleon-nucleon potentials, as well as different prescriptions for handling the reaction mechanisms in tensor polarization observables in the low  $Q^2$  region [7]. Although it is difficult to disentangle reaction mechanisms from NN potentials using cross section measurements, previous low  $Q^2$  results have indicated that asymmetries are far less sensitive to the reaction mechanisms [8]. Similar calculations have recently been finalized for the  $D(e, e'p)n$  at high  $Q^2$ , high  $p_m$  experiment [9].

Additionally, measuring  $A_{zz}$  in the quasi-elastic region will fill a gap in measurements performed on deuterium scattering. It is directly proportional to the elastic deuteron tensor analyzing powers by  $A_{zz} = \sqrt{2} [d_{20}T_{20} + d_{21}T_{21} + d_{22}T_{22}]$ . Due to the large acceptance of the SHMS spectrometer, we will be taking data in the  $x = 2$  elastic range as well, allowing us to measure  $T_{20}$  at a large range in  $Q^2$  (as contributions from  $T_{21}$  and  $T_{22}$  are small). In the deep inelastic region,  $A_{zz}$  will soon be measured to extract the tensor structure function  $b_1$  by the relation  $A_{zz} \propto \frac{b_1}{F_1}$ . Not only will measuring  $A_{zz}$  in the quasi-elastic region provide information necessary for understanding the fundamental properties of the deuteron, but it will be the first experiment to bridge a gap in measurements of electron scattering from tensor-polarized deuterons. We emphasize that this

measurement is pushing the limits of understanding the deuteron by going to kinematics where no current measurements exist and where current theoretical understanding remains unsatisfying.

## 1.1 Probing the Deuteron Wavefunction

It was suggested for some time [10] that to resolve the microscopic structure of nuclei one needs to study scattering at sufficiently large momentum transfer and large relative momenta of the produced nucleons. This logic was confirmed [4] by a series of experiments at SLAC [11] and JLab [12, 13] that directly observed short-range correlations (SRC) in a series of nuclei, and established a similar effect of SRC in the deuteron and in heavier nuclei with  $pn$  correlations giving the dominant contribution. Hence, the deuteron serves as a “hydrogen atom” for the studies of the microscopic short-range structure of the nuclei since it is the simplest nuclei that follows SRC scaling.

To achieve further progress, it is necessary to improve our knowledge of the deuteron wave function at high momenta, and to separate the S and D contributions to the high momentum component of the deuteron. The dominance of the D-wave at a large range of the nucleon momenta is expected in a range of the theoretical models, as demonstrated in Fig. 1, but experimentally it was probed in a rather indirect way via measurement of  $T_{20}$  for the deuteron form factor [14]. Still, the knowledge of S/D ratio for large momenta is rather poor. Indeed, all wavefunctions are constrained by low energy data to reproduce the S/D ratio at small momenta while the overall probability of the D-wave in the deuteron differs by a factor up to 1.5, leading to a large difference of the S/D ratio at large momenta.

In the impulse approximation, the S and D-states are related to the tensor asymmetry  $A_{zz}$  by [1]

$$A_{zz} \propto \frac{\frac{1}{2}w^2(k) - u(k)w(k)\sqrt{2}}{u^2(k) + w^2(k)}, \quad (2)$$

where  $u(k)$  is the S-state wave function and  $w(k)$  is the D-state wave function. Additionally, measuring  $A_{zz}$  at lower  $Q^2$  will map out the transition from hadronic to partonic degrees of freedom.

Ratios of inclusive cross sections at  $x > 1$  has demonstrated an early onset of the scaling of the ratios when plotted as a function of the light-cone fraction of the struck nucleon momentum. As a result, the ratios provide a direct measurement of the ratio of the high momentum components in nuclei. Similarly, one can expect that in the case of scattering from the polarized deuteron we expect the early scaling for the asymmetry when plotted as a function of the minimal struck nucleon momentum or the light cone fraction in the  $A(e, e')$  case. It was observed at JLab that the scaling of the ratios set in starting at  $Q^2 \sim 1 \text{ GeV}^2$  [12] so covering the range of  $Q^2$  up to  $2 \text{ GeV}^2$  will be sufficient to measure the S/D ratios in an interesting momentum range.

It is worth noting here that in addition to comparing predictions for the different wave functions, one expects to be able to distinguish between non-relativistic and light cone quantum mechanics models. The principal difference between the models is the relation between the spectator momentum and momentum in the wave function. In the nonrelativistic model they coincide, while in the light cone model the relation is non-linear starting at  $k \sim 250 \text{ MeV}/c$ . This difference is most clearly manifested in the scattering from the polarized deuteron due to a strong dependence of the S/D ratio on the nucleon momentum.

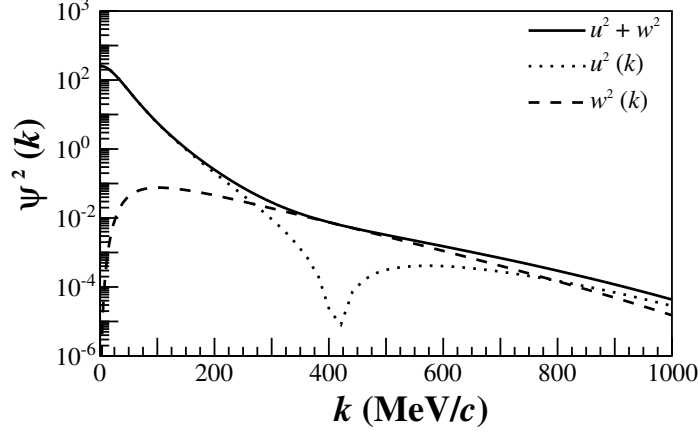


Figure 1: The AV18 [15] deuteron wave-function, showing the dominance of the D-state (dashed) in comparison to the S-state (dotted) in the full wavefunction (solid) at high momentum ( $k > 300 \text{ MeV}/c$ ).

## 1.2 Study of the Relativistic NN Bound System

One of the important issues in studying of nuclear structure at short distances is the relativistic description of the bound system. This is an important issue also in understanding the QCD medium effect with recent studies indicating that parton distribution modifications in nuclei are proportional to the high momentum component of nuclear wave function.

The deuteron is the simplest bound system and naturally any self-consistent attempt to understand the relativistic effects in the bound nuclear systems should start with the deuteron. The issue of the relativistic description of the deuteron has long history with extensive research that started in late 1970's [16, 17, 18, 10].

The experimental studies of the relativistic effects in the deuteron up to now include the large  $Q^2$  elastic  $ed$  scattering [19], however due to complexities in the reaction mechanism [20] the relativistic effects were difficult to isolate.

The inclusive  $D(e, e')X$  experiments from tensor-polarized deuterons at  $Q^2 > 1 \text{ GeV}^2$  and  $x > 1$  region gives a new possibility to probe the relativistic structure of the deuteron. In this case the use of the tensor polarized deuteron allows us to prepare the nucleus in the most compact state in which, due to the absence of the pure S-wave<sup>2</sup> contribution, the system in average is sensitive to the higher moment of the nucleon in the deuteron. At large  $Q^2 > 1 \text{ GeV}^2$  kinematics, the probed longitudinal momenta of the bound nucleon  $p_z \approx m_N(1 - x)$ , or the light cone momentum fraction  $\alpha \geq x$ . Because of these kinematic conditions and the absence of the large S-wave<sup>2</sup> contribution, one expects a measurable relativistic effects already at  $x \approx 1.2$ .

The biggest advantage is that one expects less uncertainty due to the choice of the NN potential and reaction dynamics due to relatively small values of the bound nucleon momenta involved ( $\geq 200 \text{ MeV}/c$ ).

The sensitivity to relativistic effects is estimated using the theoretical calculations based on two very different approaches. The first approach treats the virtuality of the bound nucleon within a

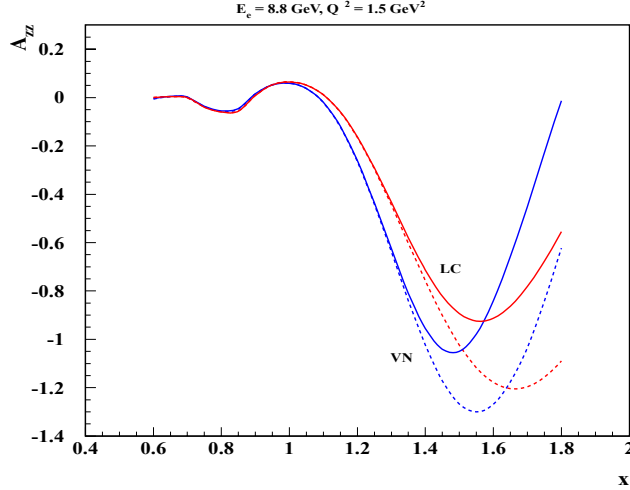


Figure 2: The  $A_{zz}$  observable calculated at  $Q^2 = 1.5 \text{ (GeV/c)}^2$  using the light-cone (red) and virtual nucleon (blue) models with NN potential inputs of AV18 (solid) and CDBonn (dotted). Calculations provided by M. Sargsian and M. Strikman [5].

description of the deuteron in the lab. frame with treating the interacting nucleon as being virtual (virtual nucleon, or VN, approximation) by taking the residue over the energy of the spectator nucleon. In this case, the deuteron wave function satisfies the covariant equation of two-nucleon bound system with spectator being on energy shell [21, 22].

Another approach is based on the observation that high energy processes evolve along the light-cone (LC). Therefore, it is natural to describe the reaction within the light-cone non-covariant framework [10]. Negative energy states do not enter in this case, though one has to take into account so called instantaneous interactions. In the approximation when non-nucleonic degrees of freedom in the deuteron wave function can be neglected, one can relate the light-cone wave functions to those calculated in the lab frame by introducing the LC  $pn$  relative three momentum,

$$k = \sqrt{\frac{m^2 + p_t^2}{\alpha(2 - \alpha)}} - m^2. \quad (3)$$

In Fig. 2, the prediction for VN [21] and LC [11] approximations are given for the highest  $Q^2$  kinematics proposed. As was previously mentioned, a measurable difference is predicted to be observable already at  $x \geq 1.2$ . to the choice of the wave function.

### 1.3 Interest from Theorists

The measurement proposed has stirred interest in a number of theorists who either have provided or are currently working on calculations. Many of these are on-going and are expected to be completed in the coming year.

The light cone and virtual nucleon calculations of M. Sargsian [23] and M. Strikman [24] are already available for  $A_{zz}$  and are presented in this document. The calculations have been done for a variety of NN potentials, indicating a discrepancy in theoretical calculations at large  $x$ .

Continuing his interest from DIS  $b_1$  calculations, W. Cosyn has developed calculations of the quasi-elastic contribution to inclusive deuteron scattering, which will be the dominant contribution in the  $x > 1$  regime [6]. His calculations, which include final-state interactions, have been modified to include  $A_{zz}$  and are presented in this proposal.

Models involving 6-quark calculations of quasi-elastic  $A_{zz}$  can be calculated by G. A. Miller [25] and have been motivated by the collaboration. In his own words, he states “This proposal really challenges theorists to better understand the meaning of nuclear wave functions in a situation that demands a relativistic treatment. I plan on working to understand this reaction during the upcoming summer.”

S. Liuti has agreed to join in the theoretical effort, stating “This is an important measurement to know, and should be calculated more thoroughly.” [26]

In addition, W. Van Orden has calculations in progress using different nucleon-nucleon potentials, as well as different prescriptions for handling the reactions mechanisms in the low  $Q^2$  region for tensor polarization observables [7]. Similar calculations have recently been done for the approved  $D(e, e'p)n$  at high  $Q^2$ , high  $p_m$  experiment [9].

In summary, we are encouraged that several theorists have engaged in serious efforts to calculate  $A_{zz}$  in the  $x > 1$  region using a variety of models.

## 2 $T_{20}$ Motivation

The elastic cross section of the deuteron is described by the charge ( $G_C$ ), magnetic ( $G_M$ ), and quadrupole ( $G_Q$ ) form factors. In order to access all three form factors, measurements are needed for both polarized and unpolarized cross sections.

In the unpolarized case, the cross section is determined by

$$\frac{d\sigma}{d\Omega} = \frac{d\sigma}{d\Omega}\bigg|_{NS} \left[ A(Q^2) + B(Q^2) \tan^2 \frac{\theta}{2} \right], \quad (4)$$

where  $A$  and  $B$  are related to the charge ( $G_C$ ), magnetic ( $G_M$ ), and quadrupole ( $G_Q$ ) form factors by

$$A = G_C^2(Q^2) + \frac{8}{9}\eta^2 G_Q^2 + \frac{2}{3}\eta G_M^2(Q^2), \quad (5)$$

$$B = \frac{4}{3}\eta(1 + \eta)G_M^2(Q^2). \quad (6)$$

The  $A$  and  $B$  form factors have been measured to high precision by many experiments, as shown in Fig. 3

In order to separate out all three form factors, a measurement of the tensor analyzing powers is also needed. Although a number of tensor analyzing powers are available,  $T_{20}$  has proven to be



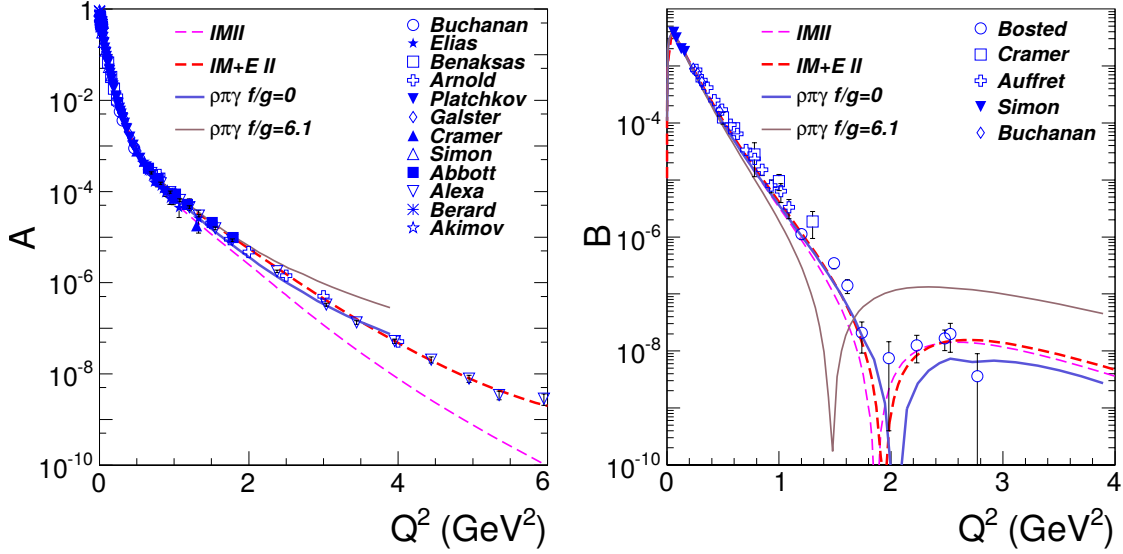


Figure 3: World data on the unpolarized deuteron form factors  $A$  and  $B$  [27].

the most informative and has been studied more indepth than the others. This analyzing power is defined by

$$T_{20} = -\frac{\frac{8}{9}\eta^2 G_Q^2 + \frac{8}{3}\eta G_C G_q + \frac{2}{3}\eta G_M^2 \left[ \frac{1}{2} + (1 + \eta) \tan^2(\theta/2) \right]}{\sqrt{2}[A + B \tan^2(\theta/2)]}, \quad (7)$$

where  $\eta = Q^2/4M^2$ , and can be measured by knowing either the initial or final polarization state. With a measurements of  $A$ ,  $B$ , and  $T_{20}$ , each of the three deuteron form factors can be extracted.

As shown in Fig. 4, the world data for  $T_{20}$  is far less well-measured than  $A$  and  $B$ . There are systematic discrepancies present between the different datasets, with measurements from JLab coming out less negative than those from Bates and VEPP-3 at higher  $Q^2 > 0.5 \text{ GeV}^2$ , which affects model calculations particularly for determining  $G_C$  [28]. Additionally, only a single experiment has been done for large  $Q^2 > 1 \text{ GeV}^2$  [29], where more data needs to be taken in order to confirm our present understanding of  $T_{20}$ .

An ideal measurement of  $T_{20}$  would be taken over a large range of  $Q^2$ , which could use the lower  $Q^2 < 0.4 \text{ GeV}^2$  results to make sure that systematic uncertainties are well understood while simultaneously measuring the region of current discrepancies ( $Q^2 \approx 0.75 \text{ GeV}^2$ ) and extending to larger four-momentum transfer to confirm the single measurement taken at  $Q^2 > 1 \text{ GeV}^2$ . By utilizing the same time-frame and kinematics that will be used to determine  $A_{zz}$ , we propose such a measurement.

### 3 The Proposed Experiment

We propose to measure the tensor asymmetry  $A_{zz}$  and tensor analyzing power  $T_{20}$  from inclusive electron scattering from polarized deuterons in the quasi-elastic and elastic region of  $0.30 < x <$

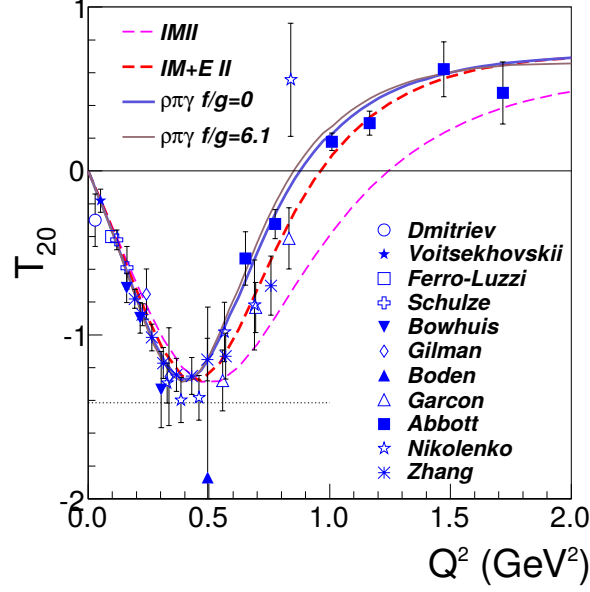


Figure 4: Existing world data on the tensor analyzing power  $T_{20}$  [27].

265  $2.0, 0.2 (\text{GeV}/c)^2 < Q^2 < 2.9 (\text{GeV}/c)^2$ , and  $1.8 < W_{NN} < 3.1 \text{ GeV}$  using the Hall C HMS and  
 266 SHMS spectrometers at forward angle using a solid polarized  $\text{ND}_3$  target.

### 267 3.1 $A_{zz}$ Experimental Method

268 The measured double differential cross section for a spin-1 target is characterized by a vector  
 269 polarization  $P_z$  and tensor polarization  $P_{zz}$  is expressed as,

$$\frac{d^2\sigma_p}{d\Omega dE'} = \frac{d^2\sigma_u}{d\Omega dE'} \left( 1 - P_z P_B A_1 + \frac{1}{2} P_{zz} A_{zz} \right), \quad (8)$$

270 where,  $\sigma_p$  ( $\sigma_u$ ) is the polarized (unpolarized) cross section,  $P_B$  is the incident electron beam polar-  
 271 ization, and  $A_1$  ( $A_{zz}$ ) is the vector (tensor) asymmetry of the virtual-photon deuteron cross section.  
 272 This allows us to write the polarized tensor asymmetry with positive tensor polarization using an  
 273 unpolarized electron beam as

$$A_{zz} = \frac{2}{P_{zz}} \left( \frac{\sigma_p - \sigma_u}{\sigma_u} \right). \quad (9)$$

274 The tensor polarization is given by

$$P_{zz} = \frac{n_+ - 2n_0 + n_-}{n_+ + n_- + n_0}, \quad (10)$$

275 where  $n_m$  represents the population in the  $m_z = +1, -1$ , or 0 state.

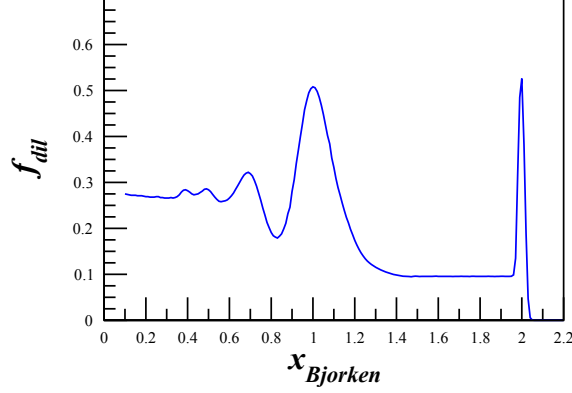


Figure 5: The estimated dilution factor, in this case at  $Q^2 = 1.5 \text{ (GeV/c)}^2$ , is expected to drop off at high  $x$  until it reaches the SRC plateau region and then the elastic peak at  $x = 2$ . The low dilution factor of  $1.1 < x < 1.95$  will be counteracted by using a high-luminosity target.

Eq. 9 reveals that the asymmetry  $A_{zz}$  compares two different cross sections measured under different polarization conditions of the target: positively tensor polarized and unpolarized. To obtain the relative cross section measurement in the same configuration, the same target cup and material will be used at alternating polarization states (polarized vs. unpolarized), and the magnetic field providing the quantization axis will be oriented along the beamline at all times. This field will always be held at the same value, regardless of the target material polarization state. This process, identical to that used for the E12-13-011  $b_1$  measurement, ensures that the acceptance remains consistent within the stability ( $10^{-4}$ ) of the super conducting magnet.

Since many of the factors involved in the cross sections cancel in the ratio, Eq. 9 can be expressed in terms of the charge normalized, efficiency corrected numbers of tensor polarized ( $N_p$ ) and unpolarized ( $N_u$ ) counts,

$$A_{zz} = \frac{2}{fP_{zz}} \left( \frac{N_p - N_u}{N_u} \right). \quad (11)$$

The dilution factor  $f$  corrects for the presence of unpolarized nuclei in the target and is defined by

$$f = \frac{N_D \sigma_D}{N_N \sigma_N + N_D \sigma_D + \sum_A N_A \sigma_A}, \quad (12)$$

where  $N_D$  is the number of deuterium nuclei in the target and  $\sigma_D$  is the corresponding inclusive double differential scattering cross section,  $N_N$  is the nitrogen number of scattered nuclei with cross section  $\sigma_N$ , and  $N_A$  is the number of other scattering nuclei of mass number  $A$  with cross section  $\sigma_A$ . As has been noted in previous work [1], the dilution factor at high  $x$  drops off considerably until the SRC plateau region, as shown in Fig. 5. By using a high-luminosity solid target and a low scattering angle  $\theta_{e'}$ , this effect will be counteracted. The dilution factor is a much smaller problem for elastic scattering at  $x = 2$ .

The dilution factor can be written in terms of the relative volume ratio of ND<sub>3</sub> to LHe in the target cell, otherwise known as the packing fraction  $p_f$ . In our case of a cylindrical target cell oriented along the magnetic field, the packing fraction is exactly equivalent to the percentage of the cell length filled with ND<sub>3</sub>.

If the time is evenly split between scattering off of polarized and unpolarized ND<sub>3</sub>, the time necessary to achieve the desired precision  $\delta A$  is:

$$t = \frac{N_p}{R_p} + \frac{N_u}{R_u} = \frac{8}{f^2 P_{zz}^2} \left( \frac{R_p(R_u + R_p)}{R_u^3} \right) \frac{1}{\delta A_{zz}^2} \quad (13)$$

where  $R_{p(u)}$  is the polarized (unpolarized) rate and  $N_{p(u)}$  is the total estimated number of polarized (unpolarized) counts to achieve the uncertainty  $\delta A_{zz}$ .

## 3.2 $T_{20}$ Experimental Method

A measurement of  $T_{20}$  will be extracted from  $A_{zz}$  on the elastic peak for each  $Q^2$  mentioned in Section 3.3. We will follow the method described by the NIKHEF measurements [30], which also used a tensor polarized target. Our methods differ in that we will use the high resolution of the HMS and SHMS to determine the elastic peak through kinematic cuts, where NIKHEF utilized a second spectrometer for that purpose.

The analyzing powers of a tensor-polarized target are described by the cross-section

$$\sigma = \sigma_0 \left[ 1 + \frac{A_d^T P_{zz}}{\sqrt{2}} \right], \quad (14)$$

where

$$A_d^T = \sum_{i=0}^2 d_{2i} T_{2i} \quad (15)$$

and

$$d_{20} = \frac{3 \cos^2 \theta^* - 1}{2}, \quad d_{21} = -\sqrt{\frac{3}{2}} \sin 2\theta^* \cos \phi^*, \quad d_{22} = \sqrt{\frac{3}{2}} \sin^2 \theta^* \cos 2\phi^*. \quad (16)$$

$\theta^*$  and  $\phi^*$  are in the frame where the  $z$  axis is along the  $\vec{q}$  and the  $x$  axis is perpendicular to  $z$  in the scattering plane, as described in [31] and shown in Fig. 6. For this proposal,  $\theta^* \approx 70^\circ$  and  $\phi^* \approx 0^\circ$ , as our target field will be oriented along the beamline and  $\theta_{\vec{q}} \approx 70^\circ$  on the elastic peak.

We rearrange Eq. 14 to be defined as our observable  $A_{zz} = \frac{2}{P_{zz}} \left( \frac{\sigma}{\sigma_0} - 1 \right)$ ,

$$A_{zz} = \sqrt{2} [d_{20} T_{20} + d_{21} T_{21} + d_{22} T_{22}], \quad (17)$$

$$T_{20} = \frac{A_{zz}}{d_{20} \sqrt{2}} - \frac{d_{21}}{d_{20}} T_{21} - \frac{d_{22}}{d_{20}} T_{22}. \quad (18)$$

Contributions from  $T_{21}$  and  $T_{22}$  are expected to be small but not negligible, and will be calculated from models that best match world data. Uncertainties from  $T_{21}$  and  $T_{22}$  are expected to be 10% and are included within the  $T_{20}$  systematic calculations.

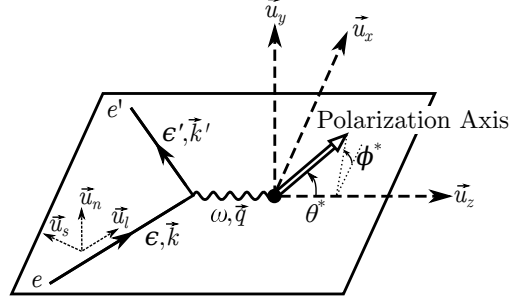


Figure 6: Coordinate system used in determining the tensor analyzing powers.

|      |      | $E_0$<br>(GeV) | $Q^2$<br>(GeV <sup>2</sup> ) | $E'$<br>(GeV) | $\theta_{e'}$<br>( $^\circ$ ) | Rates<br>(kHz) | PAC Time<br>(Days) |
|------|------|----------------|------------------------------|---------------|-------------------------------|----------------|--------------------|
| SHMS | (S1) | 8.8            | 1.5                          | 8.36          | 8.2                           | 0.38           | 25                 |
| HMS  | (H1) | 8.8            | 2.9                          | 7.26          | 12.2                          | 0.04           | 25                 |
| SHMS | (S2) | 6.6            | 0.7                          | 6.35          | 7.5                           | 3.57           | 8                  |
| HMS  | (H2) | 6.6            | 1.8                          | 5.96          | 12.3                          | 0.09           | 8                  |
| SHMS | (S3) | 2.2            | 0.2                          | 2.15          | 10.9                          | 10.5           | 1                  |
| HMS  | (H3) | 2.2            | 0.3                          | 2.11          | 14.9                          | 3.23           | 1                  |

Table 1: Summary of the central kinematics and physics rates using the Hall C spectrometers.

### 3.3 Kinematics

We propose to measure the tensor asymmetry  $A_{zz}$  for  $0.30 < x < 2.0$ ,  $0.2 \text{ (GeV/c)}^2 < Q^2 < 2.9 \text{ (GeV/c)}^2$ , and  $1.8 < W_{NN} < 3.1 \text{ GeV}$  and extract the tensor analyzing power  $T_{20}$  for  $0.2 \text{ (GeV/c)}^2 < Q^2 < 1.8 \text{ (GeV/c)}^2$ . Central kinematics of the spectrometers are given in Table 1. Fig. 7 shows the planned kinematic coverage utilizing the Hall C HMS and SHMS spectrometers at forward angles.

The polarized ND<sub>3</sub> target is discussed in Section 3.5. The magnetic field of the target will be held constant along the beamline at all times, while the target state is alternated between a polarized and unpolarized state. The tensor polarization and packing fraction used in the rates estimate are 30% and 0.65, respectively. The dilution factor in the range of this measurement is shown in Fig. 8. The spread of the elastic peak for the dilution factor was calculated assuming a momentum resolution of 0.1% for the HMS and 0.08% for the SHMS. With an incident electron beam current of 80 nA, the expected deuteron luminosity is  $1.2 \times 10^{35} \text{ cm}^{-2} \text{ s}^{-1}$ .

The momentum bite and the acceptance were assumed to be  $\Delta P = \pm 8\%$  and  $\Delta\Omega = 5.6 \text{ msr}$  for the HMS, and  $\Delta P = {}^{+20\%}_{-8\%}$  and  $\Delta\Omega = 4.4 \text{ msr}$  for the SHMS. For the choice of the kinematics, special attention was taken onto the angular and momentum limits of the spectrometers with a longitudinal polarized target: for the HMS,  $12.2^\circ \leq \theta \leq 85^\circ$  and  $1 \leq P_0 \leq 7.3 \text{ GeV/c}$ , and for the SHMS,  $5.5^\circ \leq \theta \leq 40^\circ$  and  $2 \leq P_0 \leq 11 \text{ GeV/c}$ . In addition, the opening angle between the

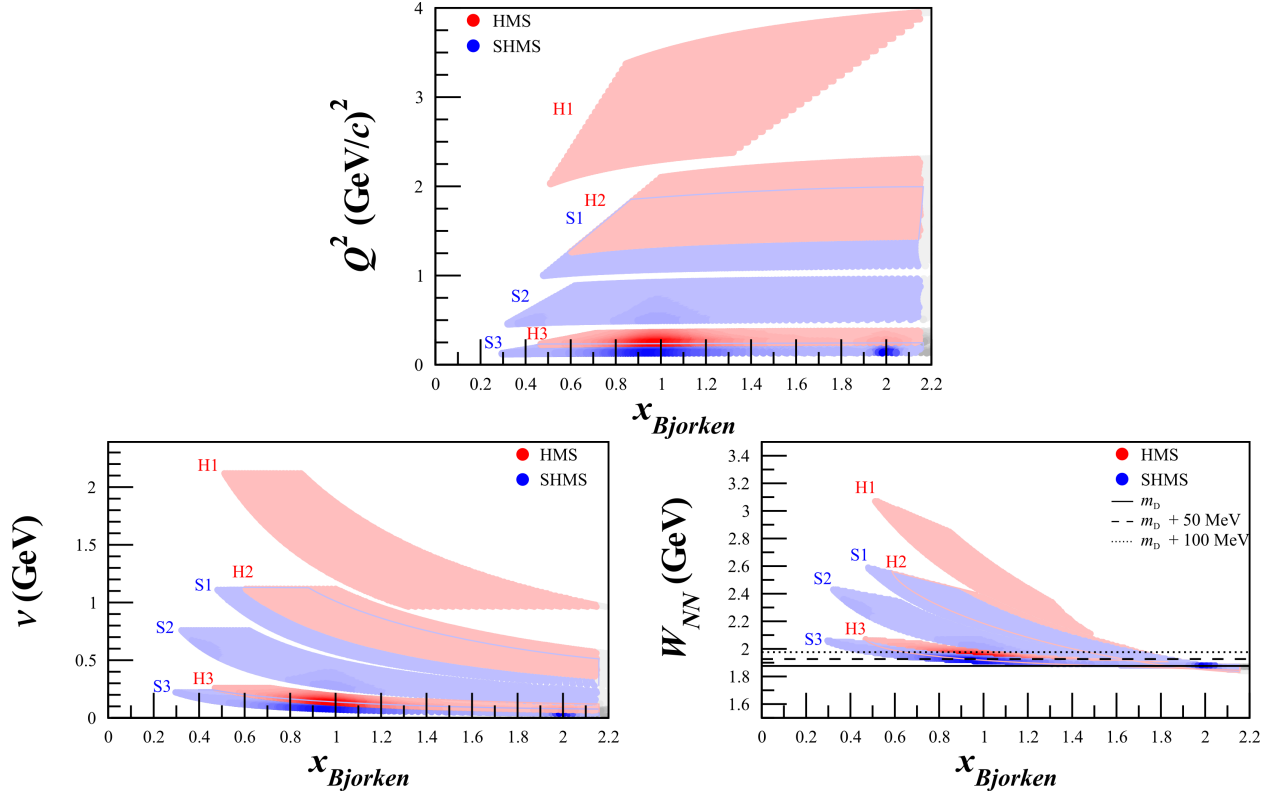


Figure 7: Kinematic coverage for central spectrometer settings at  $Q^2 = 2.9$  (GeV/c)<sup>2</sup> (H1), 1.8 (GeV/c)<sup>2</sup> (H2), 1.5 (GeV/c)<sup>2</sup> (S1), 0.7 (GeV/c)<sup>2</sup> (S2), 0.3 (GeV/c)<sup>2</sup> (H3), and 0.2 (GeV/c)<sup>2</sup> (S3). The grey regions are not included in our statistics estimates since they fall outside the range of electron-deuteron scattering. Darker shading represents areas with higher statistics. The solid, dashed, and dotted lines in the  $W_{NN}$  plot indicate deuteron mass, deuteron mass + 50 MeV, and deuteron mass + 100 MeV, respectively. Virtual-nucleon and light cone calculations are only valid for  $W_{NN} > m_D + 50$  MeV.

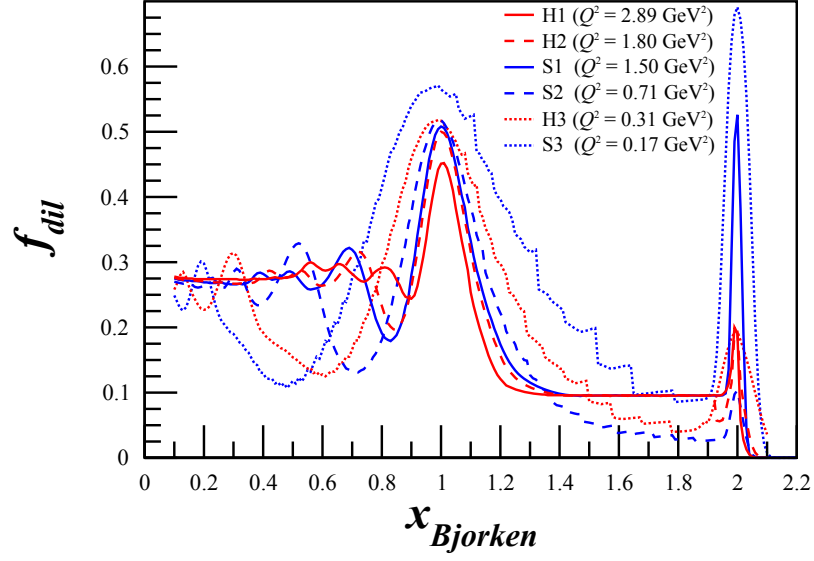


Figure 8: Projected dilution factor covering the entire  $x$  range to be measured using a combination of P. Bosted's [32] and M. Sargsian's [23] code, along with a calculation of the elastic peak using a parametrization of the deuteron form factors, for the SHMS and HMS.

spectrometers is physically constrained to be larger than  $17.5^\circ$ .

A total of 34 days of beam time is requested for production data, with an additional 10.3 days of expected overhead. The expected uncertainties, described in detail in Section 3.4, are given in Tables 2-4 and Figs. 9-11.

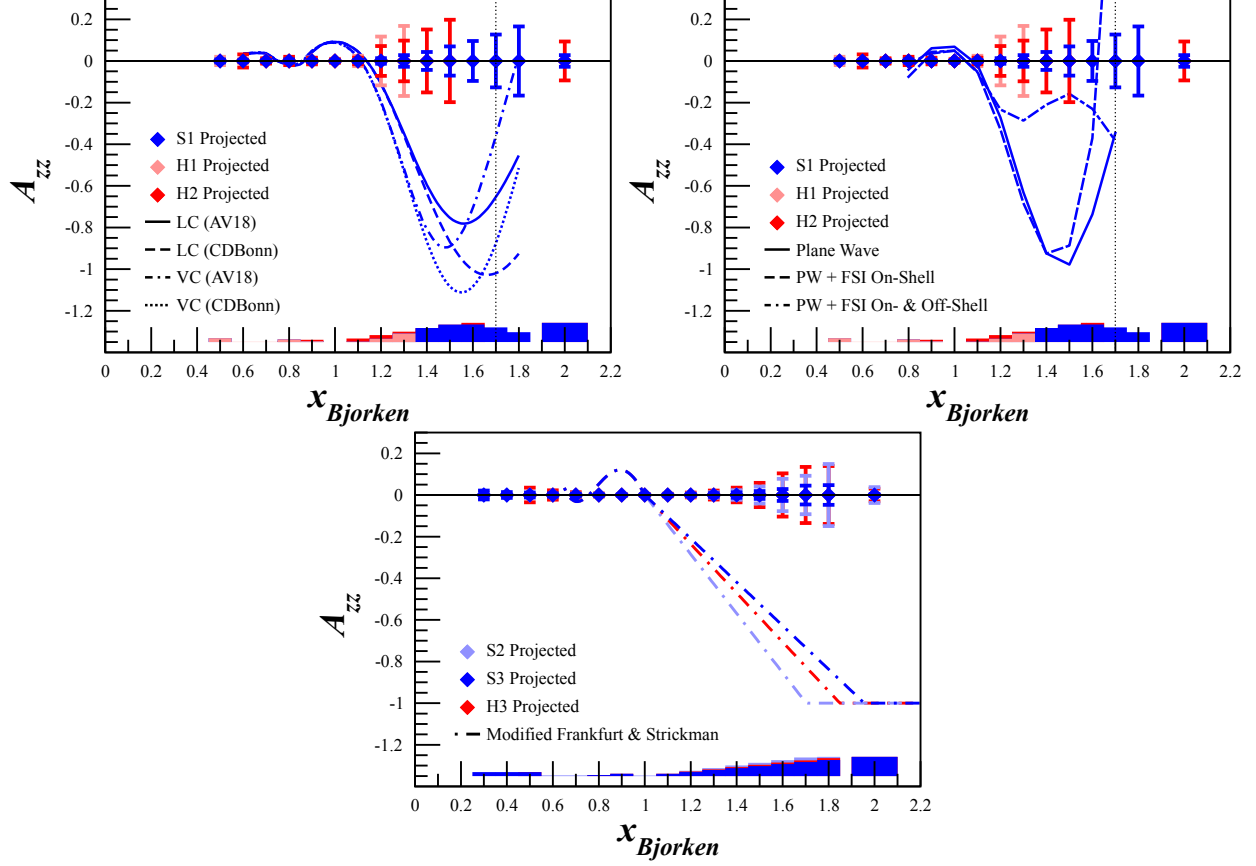


Figure 9: Projected uncertainties for the tensor asymmetry  $A_{zz}$  with 34 days of beam time. The band represents the systematic uncertainty. The top row shows the  $Q^2 > 1.0 \text{ (GeV/c)}^2$  settings and the bottom row shows the  $Q^2 < 1.0 \text{ (GeV/c)}^2$ . The upper  $x$  limit for H1 (H2) is  $x = 1.3$  ( $x = 1.5$ ). The upper-left plot includes light-cone (LC) and virtual-nucleon (VN) calculations provided by M. Sargsian [5], as well as the dependence of each model on various deuteron wave functions (AV18, CDBonn). The dotted line at  $x = 1.75$  indicates the threshold of  $W_{NN} > m_D + 100 \text{ MeV}$  where LC and VN calculations begin to not be valid as  $A_{zz}$  approaches the elastic peak [11]. The upper-right plot includes virtual-nucleon plane wave and final state interaction (FSI) calculations provided by W. Cosyn [6]. The bottom row includes a modified Frankfurt and Strickman model [1] that estimates the peak shifts in  $x$  expected due to the SRC scaling changing with  $Q^2$  [33].



|      | H1: $Q^2 = 2.9 \text{ (GeV/c)}^2$ |                                       |                                      | H2: $Q^2 = 1.8 \text{ (GeV/c)}^2$ |                                       |                                      | S1: $Q^2 = 1.5 \text{ (GeV/c)}^2$ |                                       |                                      |
|------|-----------------------------------|---------------------------------------|--------------------------------------|-----------------------------------|---------------------------------------|--------------------------------------|-----------------------------------|---------------------------------------|--------------------------------------|
| $x$  | $f_{dil}$                         | $\delta A_{zz}^{stat} \times 10^{-2}$ | $\delta A_{zz}^{sys} \times 10^{-2}$ | $f_{dil}$                         | $\delta A_{zz}^{stat} \times 10^{-2}$ | $\delta A_{zz}^{sys} \times 10^{-2}$ | $f_{dil}$                         | $\delta A_{zz}^{stat} \times 10^{-2}$ | $\delta A_{zz}^{sys} \times 10^{-2}$ |
| 0.50 | 0.29                              | 2.02                                  | 1.84                                 | —                                 | —                                     | —                                    | 0.25                              | 0.72                                  | 1.84                                 |
| 0.60 | 0.29                              | 0.91                                  | 0.10                                 | 0.27                              | 3.15                                  | 0.10                                 | 0.30                              | 0.36                                  | 0.10                                 |
| 0.70 | 0.27                              | 1.01                                  | 0.10                                 | 0.32                              | 1.26                                  | 0.10                                 | 0.29                              | 0.38                                  | 0.10                                 |
| 0.80 | 0.30                              | 1.11                                  | 1.34                                 | 0.20                              | 2.00                                  | 0.48                                 | 0.17                              | 0.74                                  | 1.34                                 |
| 0.90 | 0.24                              | 1.73                                  | 0.38                                 | 0.27                              | 1.45                                  | 1.10                                 | 0.29                              | 0.44                                  | 0.38                                 |
| 1.00 | 0.46                              | 1.03                                  | 0.10                                 | 0.50                              | 0.74                                  | 0.10                                 | 0.51                              | 0.24                                  | 0.10                                 |
| 1.10 | 0.28                              | 2.48                                  | 0.14                                 | 0.33                              | 1.58                                  | 1.65                                 | 0.34                              | 0.49                                  | 0.14                                 |
| 1.20 | 0.09                              | 11.7                                  | 1.55                                 | 0.10                              | 7.18                                  | 3.31                                 | 0.17                              | 1.34                                  | 1.55                                 |
| 1.30 | 0.11                              | 16.8                                  | 4.13                                 | 0.11                              | 9.76                                  | 4.96                                 | 0.12                              | 2.79                                  | 4.13                                 |
| 1.40 | —                                 | —                                     | —                                    | 0.12                              | 15.1                                  | 6.65                                 | 0.13                              | 4.30                                  | 6.72                                 |
| 1.50 | —                                 | —                                     | —                                    | 0.11                              | 19.8                                  | 8.29                                 | 0.10                              | 7.01                                  | 8.34                                 |
| 1.60 | —                                 | —                                     | —                                    | —                                 | —                                     | —                                    | 0.10                              | 9.60                                  | 8.42                                 |
| 1.70 | —                                 | —                                     | —                                    | —                                 | —                                     | —                                    | 0.10                              | 12.7                                  | 7.04                                 |
| 1.80 | —                                 | —                                     | —                                    | —                                 | —                                     | —                                    | 0.10                              | 16.6                                  | 4.72                                 |
| 2.00 | —                                 | —                                     | —                                    | 0.20                              | 9.33                                  | 9.20                                 | 0.50                              | 2.79                                  | 9.20                                 |

Table 2: Summary of the expected uncertainty for each  $x$  bin for settings S1, H1, and H2.

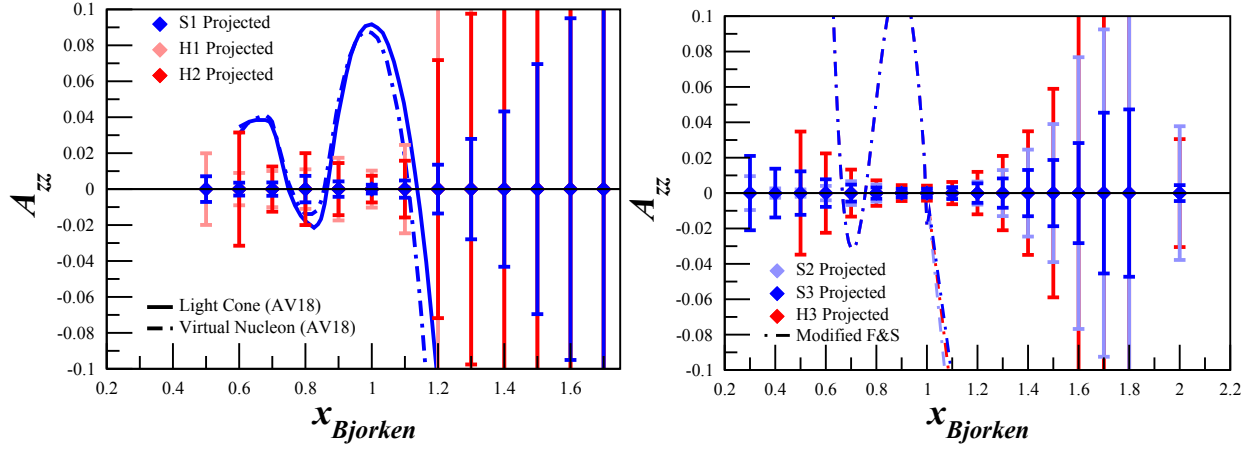


Figure 10: Projected uncertainties for the tensor asymmetry  $A_{zz}$  with 34 days of beam time, same as in Figure 9, but zoomed in to  $-0.1 < A_{zz} < 0.1$  to more clearly show the small uncertainties around the quasi-elastic peak.

| $x$  | S2: $Q^2 = 0.7 \text{ (GeV/c)}^2$ |  |   | H3: $Q^2 = 0.3 \text{ (GeV/c)}^2$ |  |   | S3: $Q^2 = 0.2 \text{ (GeV/c)}^2$ |  |   |
|------|-----------------------------------|--|---|-----------------------------------|--|---|-----------------------------------|--|---|
|      | $f_{dil}$                         | $\delta A_{zz}^{stat}$<br>$\times 10^{-2}$ | $\delta A_{zz}^{sys}$<br>$\times 10^{-2}$ | $f_{dil}$                         | $\delta A_{zz}^{stat}$<br>$\times 10^{-2}$ | $\delta A_{zz}^{sys}$<br>$\times 10^{-2}$ | $f_{dil}$                         | $\delta A_{zz}^{stat}$<br>$\times 10^{-2}$ | $\delta A_{zz}^{sys}$<br>$\times 10^{-2}$ |
| 0.30 | 0.24                              | 0.99                                       | 1.84                                      | —                                 | —  | —   | 0.18                              | 2.13                                       | 1.84                                      |
| 0.40 | 0.28                              | 0.26                                       | 1.84                                      | —                                 | —  | —   | 0.12                              | 1.38                                       | 1.84                                      |
| 0.50 | 0.32                              | 0.21                                       | 1.84                                      | 0.14                              | 3.52                                       | 1.84                                      | 0.11                              | 1.23                                       | 1.84                                      |
| 0.60 | 0.19                              | 0.41                                       | 0.10                                      | 0.12                              | 2.26                                       | 0.10                                      | 0.18                              | 0.78                                       | 0.10                                      |
| 0.70 | 0.13                              | 0.68                                       | 0.10                                      | 0.18                              | 1.33                                       | 0.10                                      | 0.28                              | 0.48                                       | 0.10                                      |
| 0.80 | 0.19                              | 0.48                                       | 0.48                                      | 0.30                              | 0.72                                       | 0.48                                      | 0.42                              | 0.31                                       | 0.48                                      |
| 0.90 | 0.39                              | 0.22                                       | 1.10                                      | 0.46                              | 0.45                                       | 1.10                                      | 0.54                              | 0.24                                       | 1.10                                      |
| 1.00 | 0.52                              | 0.16                                       | 0.10                                      | 0.52                              | 0.43                                       | 0.10                                      | 0.58                              | 0.25                                       | 0.10                                      |
| 1.10 | 0.39                              | 0.28                                       | 1.27                                      | 0.43                              | 0.63                                       | 1.07                                      | 0.53                              | 0.33                                       | 0.95                                      |
| 1.20 | 0.22                              | 0.65                                       | 2.54                                      | 0.30                              | 1.15                                       | 2.14                                      | 0.40                              | 0.55                                       | 1.91                                      |
| 1.30 | 0.14                              | 1.34                                       | 3.81                                      | 0.19                              | 2.16                                       | 3.22                                      | 0.32                              | 0.83                                       | 2.87                                      |
| 1.40 | 0.09                              | 2.29                                       | 5.06                                      | 0.14                              | 3.52                                       | 4.29                                      | 0.24                              | 1.31                                       | 3.82                                      |
| 1.50 | 0.06                              | 4.09                                       | 6.35                                      | 0.10                              | 5.85                                       | 5.37                                      | 0.20                              | 1.86                                       | 4.78                                      |
| 1.60 | 0.04                              | 7.76                                       | 7.60                                      | 0.06                              | 10.4                                       | 6.45                                      | 0.14                              | 2.87                                       | 5.74                                      |
| 1.70 | 0.04                              | 9.23                                       | 8.88                                      | 0.05                              | 13.5                                       | 7.52                                      | 0.10                              | 4.53                                       | 6.69                                      |
| 1.80 | 0.03                              | 14.9                                       | 9.20                                      | 0.06                              | 13.9                                       | 8.60                                      | 0.11                              | 4.73                                       | 7.66                                      |
| 2.00 | 0.67                              | 3.79                                       | 9.20                                      | 0.20                              | 3.05                                       | 9.20                                      | 0.70                              | 0.45                                       | 9.20                                      |

Table 3: Summary of the expected uncertainty for each  $x$  bin for settings S2, S3, and H3.

| Setting | $Q^2$<br>(GeV <sup>2</sup> ) | $\delta T_{20}^{stat}$<br>$\times 10^{-2}$ | $\delta T_{20}^{sys}$<br>$\times 10^{-2}$ |
|---------|------------------------------|--|---|
| H2      | 1.8                          | 21.7                                       | 4.74                                      |
| S1      | 1.5                          | 6.09                                       | 4.77                                      |
| S2      | 0.7                          | 8.28                                       | 6.88                                      |
| H3      | 0.3                          | 6.66                                       | 9.91                                      |
| S3      | 0.2                          | 0.99                                       | 5.59                                      |

Table 4: Expected uncertainties for  $T_{20}$  assuming a systematic uncertainty of 9.2%, which could be reduced further by utilizing the S3 measurement as a calibration for the polarized target.

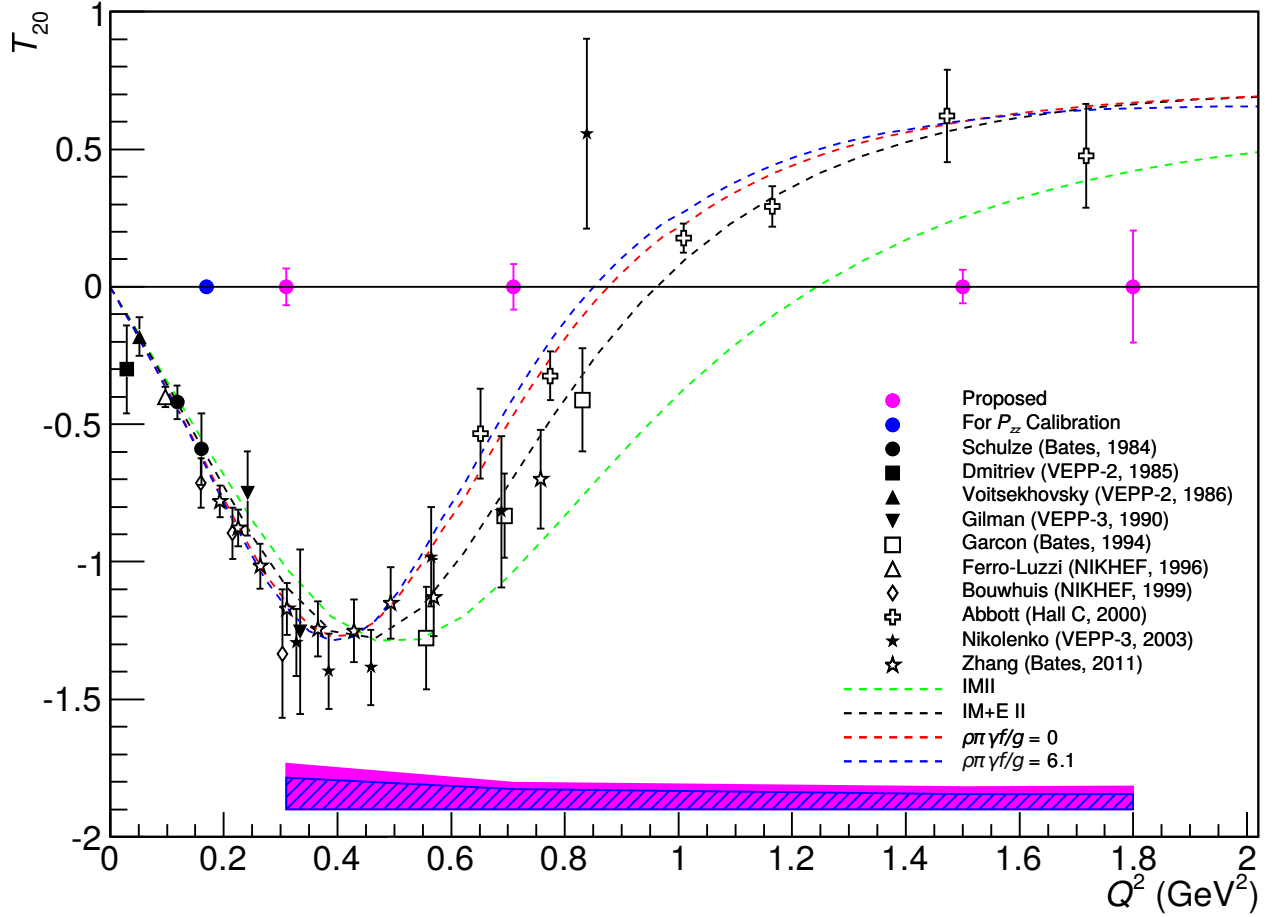


Figure 11: Projected uncertainties for the elastic tensor analyzing power  $T_{20}$  with 34 days of beam time are shown alongside the world data [27]. The point shown in blue, measured at  $Q^2 = 0.2 \text{ GeV}^2$  where  $T_{20}$  is well known theoretically and experimentally, will be used as a calibration for  $P_{zz}$ , and can potentially be used to further reduce the leading systematic uncertainty as indicated by the blue-dashed band.

### 3.4 Uncertainty Estimates

We discuss here the expected statistical and systematic uncertainties that we expect to contribute to the measurement. The projected uncertainties for  $A_{zz}$  are summarized in Tables 2-3 and displayed in Figs. 9-10. The projected uncertainties for  $T_{20}$  are summarized in Table 4 and displayed in Fig. 11.

#### 3.4.1 Statistical Uncertainty

To investigate the statistical uncertainty we start with the equation for  $A_{zz}$  using measured counts for polarized data ( $N_p$ ) and unpolarized data ( $N_u$ ),

$$A_{zz} = \frac{2}{fP_{zz}} \left( \frac{N_p}{N_u} - 1 \right). \quad (19)$$

The statistical error with respect to counts is then

$$\delta A_{zz} = \frac{2}{fP_{zz}} \sqrt{\left( \frac{\delta N_p}{N_u} \right)^2 + \left( \frac{N_p \delta N_u}{N_u^2} \right)^2}. \quad (20)$$

For  $\delta N_{p(u)} = \sqrt{N_{p(u)}}$ , the uncertainty becomes

$$\delta A_{zz} = \frac{2}{fP_{zz}} \sqrt{\frac{N_p(N_u + N_p)}{N_u^3}}, \quad (21)$$

which can't be simplified further due to the large expected asymmetry.

The number of counts was calculated using a combination of P. Bosted's [32] and M. Sargsian's [23] code for  $x < 2$ . The Bosted code was used for the lowest  $Q^2$  setting, where effects of SRC scaling are expected to be negligible, and for  $x < 1.1$  to accurately determine the quasi-elastic peak. The Sargsian code was used for the higher  $Q^2$  settings at  $x > 1.1$  due to its inclusion of SRC scaling effects.

The deuteron elastic peak was calculated using a parametrization of the deuteron elastic form factors  $A$  and  $B$  by

$$\frac{d^2\sigma}{d\Omega dE'} = \sigma_{\text{Mott}} \left( \frac{E'}{E} \right) \left[ A + B \tan^2 \left( \frac{\theta}{2} \right) \right] \delta(E' - E'_{el}), \quad (22)$$

where  $\delta(E' - E'_{el})$  is approximated by a Gaussian distribution with its width determined by the resolution of the spectrometers,

$$\delta(E' - E'_{el}) = \frac{1}{2\Delta E \cdot E'_{el} \sqrt{\pi}} e^{-\frac{(E' - E'_{el})^2}{2(\Delta E \cdot E'_{el})^2}}, \quad (23)$$

where  $\Delta E = 0.1$  (0.08)% for the HMS (SHMS) and  $E'_{el} = \frac{Q^2}{2m_D}$ . This was added to the rates calculation that was used for quasi-elastic  $A_{zz}$  and  $b_1$  [34], and the uncertainty of  $A_{zz}$  on the elastic peak was calculated the as in Eq. 21.

Following the methodology discussed in Section 3.2, we obtain the following uncertainties for  $T_{20}$ :

$$\delta T_{20}^{stat} = \frac{\delta A_{zz}^{stat}}{d_{20}\sqrt{2}}, \quad (24)$$

$$\delta T_{20}^{sys} = \sqrt{\left(\frac{\delta A_{zz}^{sys}}{d_{20}\sqrt{2}}\right)^2 + \left(\frac{d_{21}}{d_{20}}\delta T_{21}\right)^2 + \left(\frac{d_{21}}{d_{20}}\delta T_{22}\right)^2}. \quad (25)$$

### 3.4.2 Systematic Uncertainty

The spin-1 tensor-polarization dependent observables are part of the family of asymmetries which relies on obtaining data for two different target helicity states under equivalent experimental settings. A large contribution of the experimental uncertainty that effects absolute normalization cancels out as terms in the denominator and numerator are equivalent. For situations where the experimental configuration has changed during the data collection of the two different helicity states the cancellation does not occur and a rigorous accounting of the errors is required.

The tensor-polarization dependent asymmetry takes the form

$$A_{zz} = \frac{2}{fP_{zz}} \left( \frac{\sigma_p}{\sigma_u} - 1 \right), \quad (26)$$

where  $\sigma_p$  is the polarized cross section and  $\sigma_u$  is the unpolarized cross section. There are of course other spin-1 alignment dependent asymmetries, but for positive quadruple polarization in inclusive scattering all polarized observables can be expressed in terms of  $A_{zz}$ .

The figure of merit (FOM) for a tensor polarized solid state target can be defined as,

$$FOM = n_t f^2 P_{zz}^2 \quad (27)$$

where  $n_t$  is the target thickness and  $P_{zz}$  is the tensor polarization.

The contributions to the experimental uncertainty come from inaccuracies inherent in the system of measurement of the observable of interest. Each experiment contains instrumental components of systematic error which may or may not have dependence on accessible parameters. These types of errors can have a nonzero mean that changes over time so that its effect is not reduced when observations are averaged. There are also stochastic components to the uncertainty which will vary only around a single mean. There may still be a time dependence to the standard deviation of the stochastic contributions but these types of errors can be reliably estimated by repeating measurements.

Monitoring the systemic coupling of the instrumental parameters can greatly reduce the overall uncertainty produced in small asymmetry measurements. An understanding of the evolution of these types of errors over the course of the experiment can be used to make corrections after data acquisition. Reducing the time in each target spin orientation can also significantly reduce the impact of shifts in normalization. However, the stochastic components must be regulated prior to and during the experiment. Helicity flips can not reduce this type of uncertainty contribution.

Many of the errors that arise from limitations in measurement capacity have a statistical probability distribution that can be accurately estimated. For many of these types of uncertainties it

| Source                             | $A_{zz}$ Systematic | $T_{20}$ Systematic |
|------------------------------------|---------------------|---------------------|
| Polarization                       | 6.0%                | 6.0%                |
| Dilution factor                    | 6.0%                | 2.5%                |
| Packing fraction                   | 3.0%                | 3.0%                |
| Trigger/Tracking Eff.              | 1.0%                | 1.0%                |
| Acceptance                         | 0.5%                | 0.5%                |
| Charge Determination               | 1.0%                | 1.0%                |
| Detector resolution and efficiency | 1.0%                | 1.0%                |
| Total                              | 9.2%                | 7.4%                |

Table 5: Estimates of the scale dependent contributions to the systematic error of  $A_{zz}$  and  $T_{20}$ .

is possible to derive confidence limits on the domain of the measured value resulting in a relative contribution to the total systematic error. Under an independent error assumption these relative contributions add in quadrature, with polarization being the dominating uncertainty in the spin dependent observables. The standard law of combination of errors does not work when there are correlations between these types of uncertainties. For this situation the full covariance matrix is required and a minimization procedure maybe needed to keep the error under control. This is only relevant for dominant errors. For multiple kinematic tracking variables strict estimation and handling of each uncertainty is essential for a complete analysis. In many cases one may wish to assume 100% correlation between variables to simplify the book keeping for smaller contributions.

Errors are often assumed to have a normal distribution. In reality measurement errors are rarely distributed in a true Gaussian and usually have some prominent non-Gaussian tail. Given a sufficient number of measurements the central limit theorem can be employed to ensure that the estimated parameters will be more Gaussian than the estimated measurements.

Table 5 shows a list of the scale dependent uncertainties contributing to the systematic error in  $A_{zz}$ .

Polarization error is well understood and steps will be taken to minimize these contributions, as has been done in previous experiments [35]. There are additional uncertainties that can arise from RF quadrupole polarization enhancement, but recent efforts by the UVA target group to study the tensor-enhanced NMR line-shape indicate that the total uncertainty in this case can be held under 6% [36, 37].

The dilution factor  $f$  varies as a function of scattered electron energy, particularly at kinematics where nucleon resonances are prominent. The dilution factor must be known precisely at each kinematic point. This factor must be based on empirical information with measurable error, which will be measured multiple times at each kinematic setting. Though the loss to the figure of merit can easily be recovered for lower  $f$ , the error calculated from the variation of the models is only a crude estimate.

The other uncertainties in Table 5 are very standard contributions which are difficult to reduce beyond the listed instrumental lower limit.

### 3.4.2.1 Time Dependent Factors

Eq. 26 involves the ratio of counts, which leads to cancellation of several first order systematic effects. However, the fact that the two data sets will not be taken simultaneously leads to a sensitivity to time dependent variations which will need to be carefully monitored and suppressed when possible. To investigate the systematic differences in the time dependent components of the integrated counts, the effects from calibration, efficiency, acceptance, and luminosity between the two polarization states must be considered. In order to look at the effect on  $A_{zz}$  due to drifts in beam current measurement calibration and detector efficiency, Eq. 26 is rewritten explicitly in terms of the raw measured counts  $N_1$  and  $N$ ,

$$\begin{aligned} A_{zz} &= \frac{2}{fP_{zz}} \left( \frac{N_1^c}{N^c} - 1 \right) \\ &= \frac{2}{fP_{zz}} \left( \frac{Q\varepsilon l\mathcal{A}}{Q_1\varepsilon_1 l\mathcal{A}} \frac{N^1}{N} - 1 \right) \end{aligned} \quad (28)$$

where  $Q$  represents the accumulated charge, and  $\varepsilon$  is the detector efficiency. The target length  $l$  and acceptance  $\mathcal{A}$  are identical in both states, to first order.

We can then express  $Q_1$  as the change in beam current measurement calibration that occurs in the time it takes to collect data in one polarization state before switching such that  $Q_1 = Q(1 - \delta Q)$ . In this notation,  $\delta Q$  is a dimensionless ratio of charges in the different polarization states. A similar representation is used for drifts in detector efficiency leading to,

$$A_{zz} = \frac{2}{fP_{zz}} \left( \frac{N_1 Q (1 - \delta Q) \varepsilon (1 - \delta \varepsilon)}{N Q \varepsilon} - 1 \right). \quad (29)$$

which leads to,

$$A_{zz} = \frac{2}{fP_{zz}} \left( \frac{N_1}{N} (1 - \delta Q - \delta \varepsilon + \delta Q \delta \varepsilon) - 1 \right). \quad (30)$$

Estimates of  $\delta Q$  and  $\delta \varepsilon$  can be obtained from previous experiments. For the HRS detector drift during the JLab transversity experiment E06-010, the detector response was measured such that the normalized yield for the same condition over a three month period indicated little change ( $< 1\%$ ). These measurements indicated that for the short time (20 minutes) between target spin flips, the detector drift should be less than 1% times the ratio of the time period between target spin flips and three months. Also considering the period between target polarization states to be  $\approx 12$  hours leading to an overall drift  $\delta \varepsilon \sim 0.01\%$ . A similar approach can be used to establish an estimate for  $\delta Q$  using studies from the g2p/GEp experiment, resulting in  $\delta Q \sim 0.01\%$ . The SANE experiment with a beam current of 100 nA also provides some information. In this case, the relative stability of the current monitors is on the order of  $1 \times 10^{-3}$ , showing oscillations with a period of about an hour.

Expressing  $A_{zz}$  in terms of the estimated experimental drifts in efficiency and current measurement,

$$A_{zz} = \frac{2}{fP_{zz}} \left( \frac{N_1}{N} - 1 \right) \pm \frac{2}{fP_{zz}} \delta \xi. \quad (31)$$

455 where  $\delta\xi = \delta Q + \delta\varepsilon$ . This leads to a contribution to  $A_{zz}$  on the order of  $1 \times 10^{-3}$ ,

$$dA_{zz}^{drift} = \pm \frac{2}{fP_{zz}} \delta\xi = \pm 3.7 \times 10^{-3}. \quad (32)$$

456 Using the standard dilution factor and classically accessible polarization, the precision required  
457 in the raw  $A_{zz}$  measurement for already-approved DIS  $b_1$  experiment is

$$\delta A_{zz}^{raw} = \frac{fP_{zz}}{2} \delta A_{zz} = 1.5 \times 10^{-4}. \quad (33)$$

458 For this proposed  $A_{zz}$  measurement,  $f$  is changing with  $x$  significantly. For  $x \sim 1$  the dilution  
459 is greater ( $f \sim 0.5$ ) than for the larger  $x$  ( $f \sim 0.1$ ), where the large signal size indicated by  $A_{zz}$   
460 model calculations requires considerably less precision. The critical point is  $x \sim 0.8$  where  $f$  is  
461 less than 0.2 such that

$$\delta A_{zz}^{raw} = \frac{fP_{zz}}{2} \delta A_{zz} = \frac{(0.19)(0.2)}{2} (0.05) = 1.0 \times 10^{-3}. \quad (34)$$

462 So even this most sensitive point is still around an order of magnitude less constrained than the  $b_1$   
463 measurement.

464 Detector efficiencies can drift for a variety of reasons, including fluctuations in gas quality,  
465 high voltage drift, or drifts in the spectrometer magnetic fields. All of these types of variation  
466 can be controlled and minimized during the experiment through careful monitoring as well as  
467 systematic studies of the data collected. The identical configuration of the two polarization states  
468 minimizes the relative changes in luminosity with respect to time. Consistency checks on the  
469 measured cross section data can be implemented to ensure the quality of each run used in the  
470 asymmetry analysis. Fluctuations in luminosity due to target density variation can be kept to  
471 a minimum by keeping the material beads at the same temperature for both polarization states  
472 through control of the microwave and the liquid helium (LHe) evaporation. The helium vapor  
473 pressure reading provides an accuracy of material temperature changes at the level of  $\sim 0.1\%$ .  
474 Beam rastering can also be controlled to a high degree.

475 The dominant source of any variation in acceptance  $\mathcal{A}$  from state to state will be the stability  
476 of the target magnetic field. The capacity to set and hold the target super conducting magnet to a  
477 desired holding field is  $\delta B/B = 0.01\%$ . The same target cup will be used for each state, which  
478 removes any variation in the target length  $l$ .

#### 479 **3.4.2.2 Drift Mitigation**

480 Uncertainty in the measuring devices (or resulting normalization deviations) must be small  
481 compared to the scale of the asymmetry at the helicity reversal frequency. The beam noise that  
482 can contribute to these normalization deviations comes from beam current, beam position, beam  
483 energy, beam size (consistent rastering), and beam halo. Detectors drifts in photomultiplier tube  
484 (PMT) gain can change the number of events above a discriminator threshold, which can become  
485 critical when the device PMT behavior changes significantly between helicity states. This is also  
486 true for drift chamber efficiency, spectrometer analyzing field, atmospheric pressure and tempera-  
487 ture all affect these systems. The target holding field stability should never be an issue.



The most obvious way to improve the experiment considering these contributions is to increase the helicity flip frequency. Probably the most practiced way to do this is to use two different target cells alternating the cell position between a polarized target cell and an unpolarized target cell. By doing this additional uncertainties from using different packing fractions, effective target densities, and target nuclear-chemical compositions are introduced that would not be present when using identical targets for each helicity state. These contributions maybe able to be mitigated by alternating which cell is polarized. It is possible to polarize a particular cell without being in beam having it outside the homogeneous portion of the target field (beam line). In this way a target cell helicity can be prepared while taking data on the other cell. This could potential allow multiple helicity changes in a 24 hour period.

In addition to greater frequency in helicity changes, the initial polarization build-up can also be enhanced. It is possible to install an electrically controlled microwave attenuator which will allow a larger amount of microwave power to dump into the target material to speed up polarization. The attenuator can then be adjusted to the required power to sustain polarization with the addition of the electron beam.

The uncertainty estimate in charge that results in a small absolute change in the observable is described in the proposal in the Section 3.4.2.1. Analytically there is a component of uncertainty that propagates with the other relative errors and only a very small piece that results in a drift in the observable. The resulting expression for the charge and other contributions to the drift in the observable is expressed as,

$$\delta A_{zz}^d = \pm \frac{2}{f P_{zz}} \delta \xi, \quad (35)$$

where  $\delta \xi$  contains the sum of  $\delta Q$ ,  $\delta \epsilon$ ,  $\delta l$ , and  $\delta A$ . This means that to accurately represent  $\delta A_{zz}^d$  we must obtain only the residual deviation from the two polarization states in the time span of a single cycle (sampling of that data point). The value used for  $\delta Q$  is an estimate based on the actual effect seen in an observable which helps us to separate the relative contribution from the drift in a given time frame.

**3.4.2.3 Trigger-Tracking** For the most part, an easy way to determine whether or not drift will lead to an effect on the error is to determine if the change over time is seen in one polarization state and not the other with respect to the observable. Effects from trigger, cuts, and tracking efficiency do lead to errors in normalization, however both polarization states see the same stochastic fluctuation over the course of a cycle leading only to a small relative uncertainty in the observable. Aspects of the error that are non-stochastic and follow an unknown trend have been estimated in the proposal under the name ‘detector drifts.’ A secondary estimate was obtained based on HRS detector stability using Hall A transversity data for detected pions. The resulting drift was  $2.2 \times 10^{-4}$ . The detector thresholds will be set conservatively while using meticulous on-line monitoring and checks to the relative changes in tracking efficiency between slugs. For our present estimate including trigger, tracking, cuts, and detector errors that show up strictly as contributions to  $\delta \xi$ , we estimate no larger than  $2.2 \times 10^{-4}$ .

#### 3.4.2.4 Target Dilution and Length

There are presently UVA designs for target cup and material fabrication to minimize the probability of changes to target dilution in the form of material loss over time. The cup contains multiple hole arrays that are only a 0.1 mm in size. The material shape and consistency is optimized to maximize the packing fraction and minimize the fracturing capacity. The ammonia is hand selected to reduce the structural faults to obtain beads approximately 2 mm in diameter which have already undergone multiple steps of mechanical stress including being pre-irradiated at NIST with a 10  $\mu$ A beam. The temperature and thus the density of the target is kept the same in both polarized and unpolarized states. There are four temperature sensors in a standard solid polarized target setup that can be used to monitor this. The temperature is controlled via LHe evaporation, microwave, and beam heating. All three are used to maintain consistent temperature in both polarization states.

The polarized material to be used in the experiment will be contained in 3 cm long, 2.54 cm diameter cylinder cups with their axes parallel to the beam. The cylinders fit inside the 4 cm diameter vertical cylindrical tail piece at the bottom of the refrigerator. The tail piece is full of liquid helium to about 20 cm above the beam level. The heat and radiation of the beam is distributed uniformly over the cross section of the target normal to the incident beam by a combination of slow and fast rasters. The fast raster normally is a 2mm by 2mm square shape, traced by the sub-millimeter beam at kHz rates. The slow raster normally is a 1 cm maximum radius spiral, traced at constant tangential speed, covering the rastered area with 5% dose uniformity at 30 Hz and can be synchronized to the usual helicity flip signals [38].

The averaging of the target length done by the rasters results in an effective length that is determined by the fraction of the cup volume (equivalently, the rastered volume) that is filled with ammonia [38]. A possible change in the effective target length between the polarized and unpolarized periods of a measurement cycle could come from a net change of material in the raster volume. Since the raster diameter is 25% smaller than the cup diameter, there is always material outside the raster region that would fill in an unlikely loss in the rastered region. A possible estimate of the length change can be obtained by considering the ratio of the 0.008 cm<sup>3</sup> volume of a fragment to the 6.8 cm<sup>3</sup> raster volume (including packing fraction) the ratio is  $\sim 1/850$ .

The only documented instance with ammonia polarized targets and CEBAF  $\sim 100$  nA beams of a possible rearrangement of material about the target NMR coil that might indicate an associated net change in material was seen during E07-003 (SANE) which took about 500 hours of  $\geq 85$  nA beam. During one 20 h polarized and unpolarized cycle, the loss of 1 or 2 fragments would result in a  $\sim 1 \times 10^{-3}$  change in target length, with a  $\sim 20\text{h}/500\text{h}$  probability. No instances of material fragmentation, which could potentially lead to net losses in the raster region have been observed with up to 150 nA CW CEBAF beams (E93-026, E01-006, E07-003). In addition, there are checks in NMR data that can be used to ensure that no loss of a target fragments occurred between cycles.

The only instances of material fragmentation for ammonia targets were observed at SLAC, in the E143/E155/E155x series of experiments, but the SLAC beam is pulsed, with 4  $\mu$ s wide pulses of  $\sim 20$   $\mu$ A current at 120 Hz repetition rate. Such beam time structure can be expected to damage the ammonia crystals by thermal shock. In fact, to further prevent possible shock effects at JLab, the polarized target experiments in Hall C implemented the procedure of gradual ramping up of the beam current after beam trips.

All changes to the material that occur during movement of the target ladder or annealing can only happen at the end of each pair of measurement cycles and are irrelevant for the preceding or following cycles. Small changes to material NMR loop coupling are consistent to both polarization states and exist as a relative error in the polarization. In addition, as long as the LHe is superfluid ( $< 2$  K), its flow can not lead to material rearrangements. The LHe that is fed at the bottom of the nose piece coming from the separator is below 2 K, so emptying and refilling does not have any effect.

Depolarization using LHe is a relatively standard technique. In this procedure, the beam is turned off and the LHe fill valve that controls the LHe level that surrounds the target insert is slowly reduced as to not replenish the LHe evaporation until the material has warmed up and the polarization has died out. The LHe is gradually filled again as in the standard evaporation mode and again set on automated control. Once the material is unpolarized and again submerged under the LHe the microwaves are turned on in off-resonance mode. The unpolarized target is then ready for beam. This procedure provides a quick way to kill polarization while returning the unpolarized state to the exact condition of the polarized state. The small fluctuation in density, temperature and NMR material couple occur in both states and are a small relative error in the polarization. All other aspects that may result in addition to the drift are negligible.

For example, the target operating temperature is  $\sim 1.1 \pm 0.15$  K, well below the superfluid point. Over that range, the LHe density, changes by  $4 \times 10^{-5}$  (the density actually increases below  $\simeq 1.1$  K and increases above, by about equal amounts over the temperature interval [39]). The lattice constant of deuterioammonia [40] changes from 5.048 Å at 2 K to 5.073 Å at 77 K, corresponding to a  $1 \times 10^{-5}$  change over the  $\pm 0.15$  K interval considered above. For a 60% packing fraction, the change would be  $2.3 \times 10^{-5}$  for a 0.15 K unexpected temperature difference between polarization states. Any possible unaccounted changes in target length between the polarized and unpolarized parts of each cycle can also be monitored by recording the time dependence of the luminosity with a  $\simeq 0.5 \times 10^{-4}$  accuracy.

### 3.4.2.5 Solid Angle

The error that arises in the observable due to beam position and magnet currents over time is inherently very difficult to separate into drift and relative uncertainty. The 0.1% error over a 12 hour period is probably quite accurate, however, being that both polarization states experience the same fluctuations its likely that the majority of the uncertainty is relative. There are also concerns on acceptance due to beam position drift. Beam drift will be monitored during the experiment and accounted for during analysis. The largest part of this uncertainty is also a relative contribution to both target states. The contribution to the drift can be minimized with the feedback system built for parity experiments .

Trends that arise from dependence of yield on magnet currents in detectors are a concern related to the spectrometer acceptance. The drift effect can be made to be small, for the HRS typically less than  $10^{-4}$  for the dipole and  $10^{-3}$  for the three quads, and similarly for the HMS. The effects on the acceptance can be determined and corrected through careful analysis. Naturally, the target magnet current does not need to be changed between cycles, as the uniformity, stability, and setability pointed out in the proposal eliminate field variation between the two polarization states. The

residual drift from solid angle effects after such correction is expected to be no larger than 0.01%. This value was already accounted for in Section 3.4.2.3.

#### 3.4.2.6 Beam Current Monitors

Information has been extracted from experiment E06-010 for high current (10-15  $\mu\text{A}$ ), in which all the systematics are included in the yield studies including detector drift, acceptance drift, BCM drift and acceptance due to BPM drift. The beam charge asymmetries between two helicity states using the luminosity monitors for experiment E06-010 has been shown to be at the level of  $4 \times 10^{-5}$  with a width of  $2.3 \times 10^{-4}$ . An additional estimate on the change in the BCM calibration constant is seen in experiment E08-027 resulting in a absolute deviation of  $2.0 \times 10^{-4}$  over the course of six days. Long term drifts can be reduced by careful thermal isolation of the BCMs, however resulting trends will be need to be studied and corrections implemented.

Fluctuations in the calibration of beam current measuring devices can be well understood and mitigated. Even when calibrations are taken frequently, a small change in the BCM response over the course of a single helicity flip iteration can contribute a drift on the order of  $1 \times 10^{-4}$ . A Boosted Decision Tree regression maybe used similar to that used for the temperature dependence of the Q-meter. This would require accurate temperature monitoring of the BCM stainless steel pillbox resonant cavity in operation. Creating a heat regulating system using a fluid circulated chiller could help to both stabilize and accurately measure the temperature. Additional temperature stabilization of analog cables, and optimizing cable length maybe also help.

#### 3.4.2.7 Systematic Summary

It is essential to consider each uncertainty and each source separately as well as understand systemic coupling. This proposed  $A_{zz}$  measurement would be a great benefit to understand and minimize systematic uncertainties for small asymmetry measurements such as  $b_1$ . Having data at a large range of beam current, energy, and target types while studying beam noise and detector stability can help to build a comprehensive map of critical systematic issues. Other systematic minimization techniques can be explored during  $A_{zz}$  in addition to the systematic minimization mentioned in this proposal, which will be critical for  $b_1$  [41] and could help many other future experiments. In fact there is no better experimental opportunity to study the systematics of probing asymmetries in Hall C then  $A_{zz}$  at high  $x$ . Because of the scale of the predicted asymmetry  $A_{zz}$  for large  $x$ , the drifts that can corrupt  $b_1$  are only relevant for the lower  $x$  points, although for  $A_{zz}$  in this region a systematic error of the order of  $(1 \times 10^{-3})$  would be very good, which has an order of magnitude more leeway then for  $b_1$ .

### 3.5 Polarized Target

This experiment will use the JLab/UVa dynamically polarized solid  $\text{ND}_3$  target operated in longitudinal mode. The target is typically operated with a specialized slow raster and beamline instrumentation capable of characterizing the low current 50-100 nA beam. All of these requirements have been met previously in Hall C. The polarized target (see Fig. 12), has been successfully used in

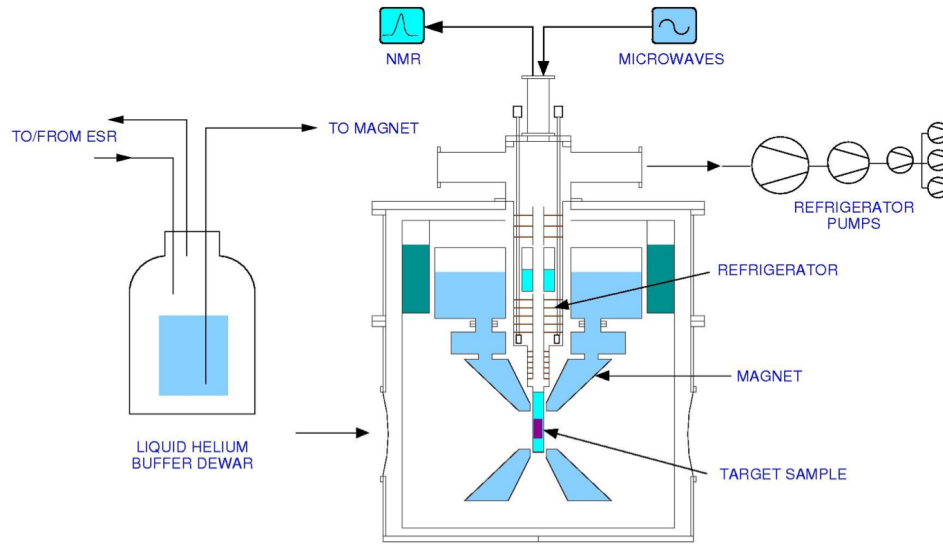


Figure 12: Cross section view of the JLab/UVa polarized target. The proposed experiment will use the modified Hall B magnet, where the backwards-scattering cone is blocked with quench protection circuitry. Figure courtesy of C. Keith.

experiments E143, E155, and E155x at SLAC, and E93-026, E01-006 and E07-003, E08-027 and E08-007 at JLab. A similar target was used in Hall B for the EG1, EG4, and DVCS experiments.

The JLab/UVa target underwent significant renovation and improvement [42] during the recent g2p run. The magnet was replaced early in the run, and the target then performed consistently. A new 1 K refrigerator and target insert were designed and constructed by the JLab target group. The cryogenic pumping system has been overhauled. In particular, the older Alcatel 2060H rotary vane pumps have been replaced with new Pfeiffer DU065 magnetically coupled rotary vane pumps, and the pump controls are being refurbished. The target motion system has been rebuilt from scratch.

The target operates on the principle of Dynamic Nuclear Polarization, to enhance the low temperature (1 K), high magnetic field (5 T) polarization of solid materials by microwave pumping. The polarized target assembly contains several target cells of 3.0 cm length that can be selected individually by remote control to be located in the uniform field region of a superconducting Helmholtz pair. The permeable target cells are immersed in a vessel filled with liquid Helium and maintained at 1 K by use of a high power evaporation refrigerator. The coils have a 50° conical shaped aperture along the beam axis which allow for unobstructed forward scattering.

The target material is exposed to microwaves to drive the hyperfine transition which aligns the nucleon spins. The heating of the target by the beam causes a drop of a few percent in the polarization, and the polarization slowly decreases with time due to radiation damage. Most of the radiation damage can be repaired by periodically annealing the target, until the accumulated dose reached is greater than about  $0.5 \times 10^{17} \text{ e}^-/\text{cm}^2$ , at which time the target material needs to be replaced.

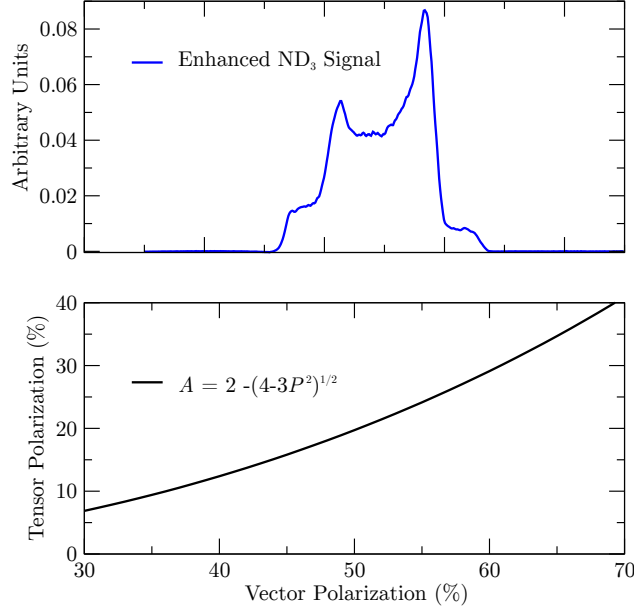


Figure 13: **Top:** NMR signal for ND<sub>3</sub> with a vector polarization of approximately 50% from the GEN experiment. **Bottom:** Relationship between vector and tensor polarization in equilibrium, and neglecting the small quadrupole interaction.

### 3.5.1 Polarization Analysis

The three Zeeman sublevels of the deuteron system ( $m = -1, 0, 1$ ) are shifted unevenly due to the quadrupole interaction [43]. This shift depends on the angle between the magnetic field and the electrical field gradient, and gives rise to two separate transition energies. Hence, the unique double peaked response displayed in Fig. 13. When the system is at thermal equilibrium with the solid lattice, the deuteron polarization is known from:

$$P_z = \frac{4 + \tanh^2 \frac{\mu B}{2kT}}{3 + \tanh^2 \frac{\mu B}{2kT}} \quad (36)$$

where  $\mu$  is the magnetic moment, and  $k$  is Boltzmann's constant. The vector polarization can be determined by comparing the enhanced signal with that of the TE signal (which has known polarization). This polarimetry method is typically reliable to about 3.9% relative.

Similarly, the tensor polarization is given by:

$$P_{zz} = \frac{4 + \tanh^2 \frac{\mu B}{2kT}}{3 + \tanh^2 \frac{\mu B}{2kT}} \quad (37)$$

From Eqs. 36 and 37, we find:

$$P_{zz} = 2 - \sqrt{4 - 3P_z^2}$$

In addition to the TE method, polarizations can be determined by analyzing NMR lineshapes as described in [44] with a typical 7% relative uncertainty. At high polarizations, the intensities

of the two transitions differ, and the NMR signal shows an asymmetry  $R$  in the value of the two peaks, as shown in Fig. 13. The vector polarization is then given by:

$$P_z = \frac{R^2 - 1}{R^2 + R + 1} \quad (38)$$

and the tensor polarization is given by:

$$P_{zz} = \frac{R^2 - 2R + 1}{R^2 + R + 1} \quad (39)$$

This measuring technique can be used as a compliment to the TE method resulting in reduced uncertainty in polarization.

### 3.5.2 Tensor Polarization Enhancement

It is possible to enhance tensor polarization using RF irradiation on the oriented deuterium nuclei to manipulate the alignment. Applying a saturating RF field on the pedestal of the smaller transition equalizes the substate  $m = +1$  and  $m = 0$  populations over 2/3 of the NMR signal. This equalization over the range of a single pedestal leads to enhancement in tensor polarization with only a small loss to the overall area ( $\sim 2\%$ ). Very recent studies at UVA using deuterated butanol have indicated that the tensor polarization can be increased by using a modified hole burning technique. The result will be investigated in the near future, and the method applied to  $\text{ND}_3$ . The studies also indicate that microwaves used during DNP does not interfere with the saturation from the RF irradiation when sufficient power is used. This implies that RF over the pedestal can be done the same time DNP is performed to enhance the area while taking beam in an experiment. Research and development is ongoing to study various techniques to optimize tensor enhancement for nuclear experiments targets.

### 3.5.3 Depolarizing the Target

To move from polarized to unpolarized measurements, the target polarization will be annihilated using destructive NMR loop field changes and destructive DNP microwave pumping. During unpolarized data taking the incident electron beam heating is enough to remove the thermal equilibrium polarization.

We are able to verify that the target is in the unpolarized state via NMR measurements. The target material will be kept at 1 K for polarized and unpolarized data collection, and the target field will be held constant for both states as well. These consistencies are used to minimize the systematic differences in the polarized and unpolarized data collection. To minimize systematic effects over time, the polarization condition will be switched twice in a 72 hour period, as shown in Fig. 15. This will be sufficient to account for drift in integrated charge accumulation.

### 3.5.4 Dilution Factor

To derive the dilution factor, we first start with the ratio of polarized to unpolarized counts. In each case, the number of counts that are actually measured, neglecting the small contributions of the

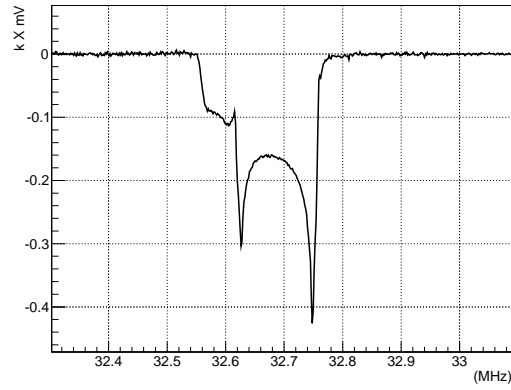


Figure 14: The deuterium magnetic resonance line shape showing the recent achievement of high tensor polarization of deuterated butanol after RF saturation of a pedestal at the UVA polarized target lab accomplished during their April 2014 cool-down.

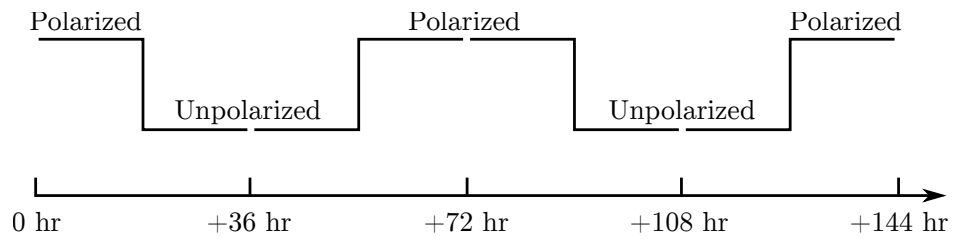


Figure 15: A visual demonstration of how the polarization cycle will happen over a 72 hour period to reduce time-dependent systematic effects. For the two lower  $Q^2$  measurements, the cycle will happen over a 18 hour period.



thin aluminium cup window materials, NMR coils, etc., are

$$N_1 = Q_1 \varepsilon_1 \mathcal{A}_1 l_1 [(\sigma_N + 3\sigma_1)p_f + \sigma_{He}(1 - p_f)], \quad (40)$$

and

$$N = Q \varepsilon \mathcal{A} l [(\sigma_N + 3\sigma)p_f + \sigma_{He}(1 - p_f)]. \quad (41)$$

where  $Q$  represents accumulated charge,  $\varepsilon$  is the dectector efficiency,  $\mathcal{A}$  the cup acceptance, and  $l$  the cup length.

For this calculation we assume similar charge accumulation such that  $Q \simeq Q_1$ , and that the efficiencies stay constant, in which case all factors drop out of the ratio leading to

$$\begin{aligned} \frac{N_1}{N} &= \frac{(\sigma_N + 3\sigma_1)p_f + \sigma_{He}(1 - p_f)}{(\sigma_N + 3\sigma)p_f + \sigma_{He}(1 - p_f)} \\ &= \frac{(\sigma_N + 3\sigma(1 + A_{zz}P_{zz}/2))p_f + \sigma_{He}(1 - p_f)}{(\sigma_N + 3\sigma)p_f + \sigma_{He}(1 - p_f)} \\ &= \frac{[(\sigma_N + 3\sigma)p_f + \sigma_{He}(1 - p_f)] + 3\sigma A_{zz}P_{zz}/2}{(\sigma_N + 3\sigma)p_f + \sigma_{He}(1 - p_f)} \\ &= 1 + \frac{3\sigma A_{zz}P_{zz}/2}{(\sigma_N + 3\sigma)p_f + \sigma_{He}(1 - p_f)} \\ &= 1 + \frac{1}{2}f A_{zz}P_{zz}, \end{aligned} \quad (42)$$

where  $\sigma_1 = \sigma(1 + A_{zz}P_{zz}/2)$  has ben substituted, per Eq. 8, with  $P_B = 0$ . It can be seen that the above result corresponds to Eq. 11.

### 3.6 Overhead

Table 6 summarizes the expected overhead, which sums to 10.3 days. The dominant overhead comes from switching from the polarized to unpolarized state and vice versa, and target anneals. The target will need to be annealed about every other day, and the material replaced once a week. Measurements of the dilution from the unpolarized materials contained in the target, and of the packing fraction due to the granular composition of the target material will be performed with a carbon target.

## 4 PAC42 Comments and Concerns

In this section we summarize the comments and concerns that were raised by the PAC42 committees on letter of intent LOI12-14-002.

### 4.1 Theory Advisory Committee

“This Letter of Intent describes a measurement of the tensor-polarized asymmetry  $A_{zz}$  in electron scattering on polarized deuterium in the quasi-elastic region, at values of  $x = 0.8 - 1.75$  ( $x$  is the equivalent Bjorken variable at the nucleon level) and

| Overhead                       | Number | Time Per (hr) | (hr)      |
|--------------------------------|--------|---------------|-----------|
| Polarization/depolarization    | 38     | 2.0           | 76.0      |
| Target anneal                  | 15     | 4.0           | 60.0      |
| Target T.E. measurement        | 6      | 4.0           | 24.0      |
| Target material change         | 4      | 4.0           | 16.0      |
| Packing Fraction/Dilution runs | 20     | 1.0           | 20.0      |
| BCM calibration                | 9      | 2.0           | 18.0      |
| Optics                         | 3      | 4.0           | 12.0      |
| Linac change                   | 2      | 8.0           | 16.0      |
| Momentum/angle change          | 3      | 2.0           | 6.0       |
|                                |        |               | 10.3 days |

Table 6: Major contributions to the overhead.

$Q^2 = 12 \text{ GeV}^2$ . The aim is to determine with this observable the  $S/D$  wave ratio in the deuteron wave function at large relative momenta  $k > 300 \text{ MeV}$ , which is important for understanding the  $NN$  interaction at short distances and the properties of the dominant  $pn$  short-range correlations in heavier nuclei. The same tensor-polarized asymmetry was/will be measured in elastic scattering (deuteron form factor) and deep-inelastic scattering (structure function  $b_1$ ); the proposed measurement in quasi-elastic scattering would fill the gap and study this observable in the region where it is most directly related to the short-range  $NN$  interaction. The tensor asymmetry at large recoil momenta also serves as a sensitive test of “relativistic effects” in the treatment of deuteron structure, which are an important aspect of the overall theoretical framework and the object of ongoing studies. A unique feature of the measurement proposed here is that it selects small-size configurations in the deuteron both through the tensor asymmetry ( $D$ -state) and the choice of kinematics ( $x > 1$ ), amplifying the overall effect. The use of  $x > 1$  for selecting small-size  $NN$  configurations has been demonstrated in previous studies of deep-inelastic structure.

The measurement proposed here arises from a well-developed context, presents a clear objective, and enjoys strong theory support. It would further explore the nature of short-range  $pn$  correlations in nuclei, the discovery of which has been one of the most important results of the JLab 6 GeV nuclear program. Development of a full proposal should be encouraged.”

## 4.2 Technical Advisory Committee

“This experiment utilizes the same apparatus and techniques as the conditionally approved b1 experiment C13-12-011. The comments in the TAC report for that experiment also apply to this experiment.

The requirement to understand and mitigate time-dependent systematic effects may be

less as the asymmetry  $A_{zz}$ , at least for  $x > 1$ , is expected to be larger than for b1. However, measuring with  $\delta A_{zz} < 0.10$  still requires a systematic control of the raw asymmetry to better than 1%. This is still challenging with a target polarization that is cycled on and off about once a day. Furthermore, at  $x > 1$ , short range structure enhances inclusive cross sections in nuclei relative to deuterium. This will reduce the dilution factor for  $x > 1$  measurements, reducing the raw asymmetries to levels where understanding and controlling systematic errors will still be important.”

### 4.3 Program Advisory Committee

**“Measurement and Feasibility:** Electron scattering off tensor-polarized deuterium would be measured in the quasi-elastic region using the Hall C HMS and SHMS spectrometers. This proposal would use the same setup as the C1-approved experiment E12-13-011, which is to measure the deuteron tensor structure function b1. The C1-approval is subject to demonstration that 35% tensor polarization is possible. The expected asymmetry is larger in the case of this measurement, but we anticipate that a similar requirement would apply. It is anticipated that a full proposal would be for 39 days, which would include 30 days for three different  $Q^2$  values and 9.1 additional days of overhead.

**Issues:** A significant amount of beam time will be required for this measurement. A full proposal will need a detail discussion of expected systematic and statistical errors similar to what is in the letter that carefully justifies the requested time. The proposal should also demonstrate what sensitivity they will have to NN interaction models, such as the 6-quark model, final state interaction models, and NN interaction models, mentioned in the proposal. It will also be important to discuss how the results will distinguish between effects from the NN-interaction, the treatment of these interactions at high virtuality, and the intrinsic deuteron wave function.

**Recommendation:** Proceed to proposal addressing the issues noted above.”

### 4.4 Response to PAC42 Concerns

The tensor polarization of 30% used in the rates for this proposal is the same as condition on the E12-13-011 proposal, which was incorrectly mentioned as 35%. To ensure that the target polarization is not significantly affected by the electron beam, we’ve reduced our estimated current from 90 nA in the LOI to 80 nA, which is the conservative standard for a DNP target. We have expanded upon our estimated statistical and systematic uncertainties in Section 3.4 and in a recent technical note [41], where we stress that a measurement of  $A_{zz}$  in the quasi-elastic and  $x > 1$  region is ideal for understanding time-dependent systematic effects without significantly affecting the measurement, as it is an order of magnitude less sensitive to drift effects than  $b_1$ . Furthermore, we will be measuring  $T_{20}$  at low  $Q^2$  where the observable is well understood both experimentally and theoretically, which can be used as a calibration and as a systematic check on the NMR measurement of the polarization. There has also been a dedicated effort made in understanding the

tensor-enhanced polarization state by the UVA group over the past few years. Through studying tensor polarization enhancement and NMR line-shape analysis over multiple cool-downs, the UVA group is confident that the uncertainty in polarization can be kept to  $< 6\%$  [36, 37]. However, even a very conservative estimate of  $12\%$ , as given in LOI12-14-002, would make for a compelling measurement.

Since PAC42, we have engaged a number of theorists who have provided calculations not only between light cone and virtual nucleon models, but also using different  $NN$  interaction potentials [5], and from on- and off-shell contributions to final state interactions (FSI) [6]. Deviations based on  $NN$  potentials and FSI only become apparent at large  $x > 1.3$ , so that the low  $x < 1.3$  region can be used to discriminate between light cone and virtual nucleon calculations. Furthermore,  $A_{zz}$  calculations based on  $NN$  potentials are currently being systematically studied at low  $Q^2$  by W. Van Orden and are expected to be completed within a year [7]. Although not completed at the time of this proposal, G. A. Miller is still engaged in providing calculations of 6 quark effects in the elastic region [25]. Additionally, the proposed  $A_{zz}$  measurements are also ideal for making simultaneous high-precision measurements of  $T_{20}$  to test existing calculations up to large  $Q^2$ , as discussed in Section 3.2, including in the region where Hall C and MIT-Bates data show a discrepancy, which requires only four more days of beam time than initially proposed in the LOI. Along with the ground-breaking measurements of  $A_{zz}$  in the  $x > 1$  region, we will also be measuring  $T_{20}$  in the largest  $Q^2$  range ever taken in a single experiment.

## 5 Summary

We have investigated the possibility of making high precision measurements of the quasi-elastic tensor asymmetry  $A_{zz}$ . By covering the kinematic range from the QE peak ( $x \approx 1$ ) up to elastic scattering ( $x = 2$ ), we expect that this data will provide valuable new insights about the high momentum components of the deuteron wavefunction. We have been actively working with several theorists who have provided state-of-the-art calculations of light cone, virtual nucleon, and final state interactions. Additional calculations are being performed that include six-quark models, and low  $Q^2$  sensitivity to NN potentials. It is important to note that this is the same kinematic region that has been shown to be correlated with the EMC effect via the  $x > 1$  A/D ( $e, e'$ ) results.

Additionally, our measurement of  $A_{zz}$  allows for a simultaneous measurement of the tensor analyzing power  $T_{20}$  without any further beam time or equipment by making a kinematic cut on the elastic peak. The lowest  $Q^2$  measurement will fall on the most experimentally probed and theoretically understood region, making it ideal for ensuring that the tensor polarized target is operating correctly and to help reduce target systematic uncertainty, the leading systematic in this experiment. At medium  $Q^2$ , our measurement will fall in the same region where there is currently a discrepancy between Hall C and Bates results. Our final point will lie at the highest  $Q^2$  value ever measured for  $T_{20}$ , and will provide a crucial test of ensuring our understanding of  $T_{20}$ . These measurements of  $T_{20}$  will also cover the largest range in  $Q^2$  measured by a single experiment.

We have found that with 34 days of beam and an additional 10.3 days of overhead,  $A_{zz}$  can be measured with high precision at  $Q^2 = 0.2, 0.3, 0.7, 1.5, 1.8$  and  $2.9$   $(\text{GeV}/c)^2$  and  $T_{20}$  at  $Q^2 = 0.2, 0.3, 0.7, 1.5$ , and  $1.8$   $(\text{GeV}/c)^2$  in Hall C using identical equipment as the upcoming  $b_1$  measure-

836 ment while being orders of magnitude less sensitive to systematic uncertainties. In addition, this  
 837 data will fill a gap in measurements of  $A_{zz}$  between the  $T_{20} \propto A_{zz}$  elastic measurements and the  
 838  $b_1 \propto \frac{A_{zz}}{F_1^d}$  deep-inelastic measurements.

## References

- [1] L. Frankfurt and M. Strikman, Phys.Rept. **160**, 235 (1988).
- [2] M. Sargsian, private communication, to be published.
- [3] J. L. Forest *et al.*, Phys. Rev. **C54**, 646 (1996).
- [4] J. Arrington, D. Higinbotham, G. Rosner, and M. Sargsian, Prog.Part.Nucl.Phys. **67**, 898 (2012).
- [5] M. M. Sargsian and M. I. Strikman, J.Phys.Conf.Ser. **543**, 012009 (2014).
- [6] W. Cosyn, private communication.
- [7] W. Van Orden, private communication.
- [8] I. Passchier, L. van Buuren, D. Szczerba, R. Alarcon, T. Bauer, *et al.*, Phys.Rev.Lett. **88**, 102302 (2002).
- [9] W. P. Ford, S. Jeschonnek, and J. Van Orden, Phys.Rev. **C90**, 064006 (2014).
- [10] L. L. Frankfurt and M. I. Strikman, Phys. Rept. **76**, 215 (1981).
- [11] L. Frankfurt, M. Strikman, D. Day, and M. Sargsian, Phys.Rev. **C48**, 2451 (1993).
- [12] J. Arrington, C. Armstrong, T. Averett, O. K. Baker, L. de Bever, *et al.*, Phys.Rev.Lett. **82**, 2056 (1999).
- [13] N. Fomin, J. Arrington, R. Asaturyan, F. Benmokhtar, W. Boeglin, *et al.*, Phys.Rev.Lett. **108**, 092502 (2012).
- [14] M. Garcon and J. Van Orden, Adv.Nucl.Phys. **26**, 293 (2001).
- [15] S. Veerasamy and W. N. Polyzou, Phys. Rev. C **84**, 034003 (2011).
- [16] F. Gross, Phys.Rev. **C26**, 2203 (1982).
- [17] W. Buck and F. Gross, Phys.Rev. **D20**, 2361 (1979).
- [18] L. Frankfurt and M. Strikman, Nucl.Phys. **B148**, 107 (1979).
- [19] L. Alexa *et al.*, Phys.Rev.Lett. **82**, 1374 (1999).
- [20] J. Van Orden, N. Devine, and F. Gross, Phys.Rev.Lett. **75**, 4369 (1995).
- [21] M. M. Sargsian, Phys.Rev. **C82**, 014612 (2010).
- [22] F. Gross and A. Stadler, Phys.Rev. **C82**, 034004 (2010).

- 866 [23] M. Sargsian, private communication.
- 867 [24] M. Strikman, private communication.
- 868 [25] G. Miller, private communication.
- 869 [26] S. Liuti, private communication.
- 870 [27] R. Holt and R. Gilman, Rept.Prog.Phys. **75**, 086301 (2012).
- 871 [28] R. A. Gilman and F. Gross, J.Phys. **G28**, R37 (2002).
- 872 [29] D. Abbott *et al.*, Phys.Rev.Lett. **84**, 5053 (2000).
- 873 [30] M. Bouwhuis, Z. Zhou, M. Ferro-Luzzi, E. Passchier, R. Alarcon, *et al.*, Phys.Rev.Lett. **82**,  
874 687 (1999).
- 875 [31] T. Donnelly and A. Raskin, Annals Phys. **169**, 247 (1986).
- 876 [32] P. Bosted and V. Mamyan, e-print **arXiv:1203.2262**, (2012).
- 877 [33] L. Frankfurt, M. Sargsian, and M. Strikman, Int.J.Mod.Phys. **A23**, 2991 (2008).
- 878 [34] E. Long *et al.*, JLab Technical note, JLAB-TN-13-029 (2013).
- 879 [35] D. Keller, Nucl. Instrum. Meth. **A728**, 133 (2013).
- 880 [36] D. Keller, PoS **PSTP2013**, 010 (2013).
- 881 [37] D. Keller, Int.J.Mod.Phys.Conf.Ser., The 21st International Symposium on Spin Physics  
882 (2014), in press.
- 883 [38] C. Yan, JLab Hall C Technical Note,  
884 [http://hallcweb.jlab.org/document/howtos/slow\\_raster.pdf](http://hallcweb.jlab.org/document/howtos/slow_raster.pdf).
- 885 [39] Russell J. Donnelly, <http://pages.uoregon.edu/rjd/vapor2.htm>.
- 886 [40] A. W. Hewat and C. Riekel, Acta Crystallographica Section A **35**, 569 (1979).
- 887 [41] D. Keller, JLab Technical note, JLAB-TN-15-014 (2015).
- 888 [42] C. Keith, JLab polarized target group. Private communication.
- 889 [43] W. Meyer *et al.*, Nucl. Instrum. Meth. **A244**, 574 (1986).
- 890 [44] C. Dulya *et al.*, Nucl. Instrum. Meth. **A398**, 109 (1997).